Monthly Notices of the ROYAL ASTRONOMICAL SOCIETY

MNRAS **541,** 2631–2650 (2025) https://doi.org/10.1093/mnras/staf1047
Advance Access publication 2025 June 28

Tracing the Milky Way: calibrating chemical ages with high-precision *Kepler* data

G. Casali [1,2,3,4★] J. Montalbán,[3,5,6] A. Miglio [3,4,6] L. Casagrande [1,2] L. Magrini [7] C. Chiappini,[8] A. Bragaglia,[4] M. Matteuzzi,[3,4] K. Brogaard [3,9] A. Stokholm [6,3,9] V. Grisoni [10,3] M. Tailo [3,11,12] and E. Willett [6]

[1]*Research School of Astronomy and Astrophysics, The Australian National University, Canberra, ACT 2611, Australia*
[2]*ARC Centre of Excellence for All Sky Astrophysics in 3 Dimensions (ASTRO 3D), Canberra, ACT 2611, Australia*
[3]*Dipartimento di Fisica e Astronomia, Università di Bologna, Via P. Gobetti 93/2, I-40129 Bologna, Italy*
[4]*INAF – Osservatorio di Astrofisica e Scienza dello Spazio, Via P. Gobetti 93/3, I-40129 Bologna, Italy*
[5]*INAF – Osservatorio Astrofisico di Catania, Via Santa Sofia, 78, I-95123 Catania, Italy*
[6]*School of Physics & Astronomy, University of Birmingham, Edgbaston, Birmingham B15 2TT, UK*
[7]*INAF – Osservatorio Astrofisico di Arcetri, Largo E. Fermi 5, I-50125 Firenze, Italy*
[8]*Leibniz-Institut fur Astrophysik Potsdam (AIP), An der Sternwarte 16, D-14482 Potsdam, Germany*
[9]*Stellar Astrophysics Centre, Aarhus University, Ny Munkegade 120, Bldg. 1520, DK-8000 Aarhus C, Denmark*
[10]*INAF – Osservatorio Astronomico di Trieste, via G.B. Tiepolo 11, I-34131, Trieste, Italy*
[11]*INAF – Osservatorio Astronomico di Padova, Vicolo dell'Osservatorio 5, Padova, IT-35122, Italy*
[12]*INAF, Observatory of Rome, Via Frascati 33, I-00077, Monte Porzio Catone (RM), Italy*

Accepted 2025 June 23. Received 2025 May 22; in original form 2024 November 27

ABSTRACT

Chemical clocks offer a powerful tool for estimating stellar ages from spectroscopic surveys. We present a new detailed spectroscopic analysis of 68 *Kepler* red giant stars to provide a suite of high-precision abundances along with asteroseismic ages with better than 10 per cent precision from individual mode frequencies. We obtained several chemical clocks as ratios between *s*-process elements (Y, Zr, Ba, La, and Ce) and α-elements (Mg, Ca, Si, Al, and Ti). Our data show that [Ce/Mg] and [Zr/Ti] display a remarkably tight correlation with stellar ages, with abundance dispersions of 0.08 and 0.01 dex, respectively, and below 3 Gyr in ages, across the entire Galactic chronochemical history. While improving the precision floor of spectroscopic surveys is critical for broadening the scope and applicability of chemical clocks, the intrinsic accuracy of our relations – enabled by high-resolution chemical abundances and stellar ages in our sample – allows us to draw meaningful conclusions about age trends across stellar populations. By applying our relations to the Apache Point Observatory Galactic Evolution Experiment (APOGEE) and *Gaia*-ESO surveys, we are able to differentiate the low- and high-α sequences in age, recover the age–metallicity relation, observe the disc flaring of the Milky Way, and identify a population of old metal-rich stars.

Key words: asteroseismology – stars: abundances – stars: late-type – Galaxy: abundances – Galaxy: disc – Galaxy: evolution.

1 INTRODUCTION

In the era of the *Gaia* satellite (Gaia Collaboration 2021), astrometric data coupled with high-resolution spectra give constraints to models of the Milky Way formation and assembly history. An important piece of information is provided by our ability to infer stellar ages and consequently to sketch a Galactic timeline. Asteroseismology can come to our aid giving us the possibility to infer precise ages of field stars, which are known to be very difficult to obtain (see Soderblom 2010, for a review). Through asteroseismology, we are able to detect solar-like pulsations in thousands of G-K giants using data collected by the *COnvection ROtation and planetary Transits* (CoRoT; Baglin et al. 2006), *Kepler* (Borucki et al. 2010; Gilliland et al. 2010), *K*2 (Howell et al. 2014), and *Transiting Exoplanet Survey Satellite* (TESS; Ricker et al. 2014) missions. The pulsation frequencies are directly linked to the stellar structure and thus provide tight constraints on stellar properties (radius, mass, and age) and evolutionary state (see Chaplin & Miglio 2013, for a review). In fact, through two global seismic parameters – the average large frequency separation ($\Delta\nu$) and the frequency of maximum oscillations power ($\nu_{\rm max}$) – stellar parameters can be deduced. Another method to get the highest levels of precision from asteroseismology is obtained when comparing observed individual mode frequencies (tens of constraints, compared to the two provided by the global seismic parameters) to stellar models (i.e. Huber et al. 2013; Lebreton & Goupil 2014; Lillo-Box et al. 2014; Davies & Miglio 2016; Silva Aguirre et al. 2017; Montalbán et al. 2021; Montalbán, in preparation). These frequencies can be measured in long time-series, such as *Kepler* (4.5 yr compared to dozen/hundreds days for the other missions). Indeed, *Kepler* light curves have allowed us to reach an unprecedented precision in stellar age for isolated field stars, similar

★ E-mail: giada.casali@anu.edu.au

to what can be done for stellar clusters (~ 20 per cent using $\nu_{\rm max}$ and $\Delta\nu$, ~ 11 per cent using individual mode frequencies, see Miglio et al. 2021; Montalbán et al. 2021, respectively).

Starting from high-quality spectra for a sample of stars with well-known ages ('calibrators', in this case stars with ages from asteroseismology), it is possible to obtain empirical relations between abundance ratios and stellar ages. The best abundance ratios are those composed of two elements produced on different time-scales due to their different nucleosynthetic sites – e.g. a slow neutron-capture element (or *s*-process element) and an α-element – resulting in a strong correlation with stellar age. In Galactic chemical evolution, abundances of different elements are produced by stars of different masses, thus with different time-scales. Indeed, *s*-process elements are mainly ejected in the interstellar medium (ISM) from low- and intermediate-mass asymptotic giant branch stars with time-scales from about 0.5 to 7 Gyr, whereas α-elements are mainly ejected in the ISM from Type II supernovae with very short time-scale less than 50 Myr. These abundance ratios are called chemical clocks and the most studied ones are [Y/Mg] and [Y/Al] (da Silva et al. 2012; Nissen 2015; Feltzing et al. 2017; Slumstrup et al. 2017; Delgado Mena et al. 2019; Casali et al. 2020; Casamiquela et al. 2021; Viscasillas Vázquez et al. 2022; Shejeelammal et al. 2024, and references therein). Although they are very promising, and show a clear relationship between age and abundance ratio for solar twins (Nissen 2015; Spina et al. 2016, 2018; Jofré, Jackson & Tucci Maia 2020; Nissen et al. 2020), recent works have shown that these empirical relations differ slightly in the inner and outer regions of the Galactic disc with respect to the solar vicinity and depend on metallicity (Feltzing et al. 2017; Delgado Mena et al. 2019; Casali et al. 2020; Magrini et al. 2021; Viscasillas Vázquez et al. 2022).

In this work, we aim to calibrate chemical clocks with a well-controlled high-quality sample of stars and transfer their age information to field stars ('test sample') in the large spectroscopic surveys, such as Apache Point Observatory Galactic Evolution Experiment (APOGEE) DR17 (Abdurro'uf et al. 2022) and *Gaia*-ESO (Randich et al. 2022). To achieve this goal, we observed 68 giants in the *Kepler* field with the High Accuracy Radial velocity Planet Searcher in North hemisphere (HARPS-N, Cosentino et al. 2012) and FIbre-fed Echelle Spectrograph (FIES, Telting et al. 2014) spectrographs to carry out a detailed chemical inventory (also complementing the APOGEE DR17 information with *n*-capture elements) coupled with asteroseismic ages determined using individual mode frequencies from Montalbán et al. (in preparation), where stellar ages for a total of ~ 5000 *Kepler* stars will be presented. In a companion paper, we will focus on the full set of chemo-age relations computed with the sample of 68 stars and compare with Galactic chemical evolutionary models (Casali et al., in preparation).

The paper is structured as follows. In Section 2, we describe the data sample, its high-precision spectroscopy analysis, the age inference, and the comparison with the APOGEE survey; calibration of chemical clocks and applications of the empirical relations are in Sections 3 and 4, respectively; finally, in Section 5, we summarize and conclude.

2 OBSERVATIONS AND DATA SAMPLE

We selected 68 stars among the *Kepler* red giant branch (RGB) stars with high-quality power spectra,[1] from the Miglio et al.'s (2021) catalogue cross-matched with the Sloan Digital Sky Survey data release 17 of the high-resolution spectroscopic survey, APOGEE (Majewski et al. 2017; Abdurro'uf et al. 2022). The selection was made taking stars in the high- and low-α sequences of APOGEE DR17, selecting the same number of stars in the two sequences over the metallicity range [Fe/H] $= [-0.8, 0.4]$ dex. Moreover, we selected stars bright enough ($G < 11$) to be observed with high-resolution spectrographs on 2–4 m telescopes.

We obtained spectra with two different instruments: HARPS-N ($R \sim 115\,000$, $\Delta\lambda = 383 - 693$ nm) at the Telescopio Nazionale Galileo (TNG) and FIES ($R \sim 67\,000$, $\Delta\lambda = 370 - 830$ nm) at the Nordic Optical Telescope (NOT), both at the Roque de los Muchachos Observatory (La Palma, Spain). The observations were conducted from 2022 July 19 to 22 and from 2023 July 25 to 27 (programmes A45TAC_22 and A47TAC_9), respectively, at the TNG and from 2022 June 24 to 26 at the NOT (proposal number: 65–006). The spectra were acquired with total exposure times ranging from 1200 to 3600 s depending on the star brightness, in order to reach a signal-to-noise ratio per pixel at blue wavelengths of S/N > 40. Exposure times longer than 1800 s were usually split into two or three subexposures to reduce the contamination of cosmic rays and to avoid saturation.

The stars analysed in this work are listed in Table 1 with their coordinates, *Gaia* magnitudes, parallax, and proper motions. Four stars were observed using both instruments to check for possible offsets in atmospheric parameters and chemical abundances caused by the use of two different spectrographs. All spectra are available from TNG and NOT archives.

2.1 Spectral analysis

We performed a spectral analysis based on the measurements of the equivalent widths (EWs) to determine the atmospheric parameters and abundances of our sample stars. The EWs of the spectral absorption lines were measured using the DAOSPEC (Stetson & Pancino 2008) tool through an automatic wrapper DOOp (Daospec Output Optimiser pipeline, Cantat-Gaudin et al. 2014). The linelist of atomic transitions used in this work was the master list prepared for the analysis of the stellar spectra for the *Gaia*-ESO survey (Heiter et al. 2015, 2021). This linelist includes three flags that provide information about the quality of the transition probabilities and the blending properties, such as 'Y' (yes), 'N' (no), and 'U' (undetermined). These flags are assigned on the basis of the accuracy of the log gf (line oscillator strength) and the quality of the line profiles (at the resolving power $R \sim 47\,000$). In our analysis, we considered all lines, except those with 'N' for the log gf values. Moreover, we selected lines with EWs between $20 - 120$ mÅ for iron and between $10 - 120$ mÅ for the other elements to avoid saturated and overly weak lines. Regarding neutron-capture elements, we considered only lines with 'Y' for the log gf values.

The EWs measured through DOOp were passed to MOOG in the automatic form: Fast Automatic MOOG Analysis (FAMA, Magrini et al. 2013). FAMA uses MOOG in its 2017 version (Sneden et al. 2012) and a grid of MARCS model atmospheres (Gustafsson et al. 2008) to determine atmospheric parameters and abundances. It iteratively searches for the effective temperature $T_{\rm eff}$ by minimizing the slope between iron abundance and the excitation potential and the microturbulence ξ by minimizing the trend between iron abundance and the reduced EWs, log(EW/λ). The log g is fixed to the seismic value computed using the scaling relation:

$$\log\ g = \log\ g_{\odot} + \log(\nu_{\rm max}/\nu_{\rm max,\odot}) + 1/2\log(T_{\rm eff}/T_{\rm eff,\odot}) \quad (1)$$

[1] The entire sample of *Kepler* RGB stars with high-quality power spectra will be published in Montálban et al. (in preparation).

Table 1. Parameters of the *Kepler* stars.

Name (KIC)	Telescope	*Gaia* DR3 ID	RA (J2000)	Dec.	Plx (mas)	μ_α (mas yr^{-1})	μ_δ (mas yr^{-1})	Gmag
1433803	NOT	2 051 703 785 658 841 600	291.72570630879	37.03846643288	2.5376	1.832	−12.493	10.15
2451509	NOT	2 051 665 607 692 314 368	293.24321361009	37.70252480197	1.667	−1.873	−9.830	9.93
2970584	TNG	2 099 962 209 991 763 456	286.03837277092	38.16971098852	1.973	7.064	−15.797	10.01
3429738	TNG	2 099 600 161 429 446 016	287.19501623686	38.59784869632	1.874	−18.696	−11.068	10.02
3539408	TNG	2 052 888 058 462 055 296	289.95602718206	38.68070416077	2.2985	−9.392	−5.065	9.64
3644223	NOT	2 052 939 086 972 190 208	291.07699505523	38.78791593017	3.1637	−8.748	−28.62	9.54
3661494	TNG	2 076 159 569 968 802 176	295.33964205499	38.72007372105	1.6322	−22.057	−7.288	10.57
3744043	TNG	2 052 864 114 022 602 496	290.6144515805	38.84814303874	2.5287	10.405	25.379	9.65
4055294	NOT	2 052 965 234 733 414 528	291.04521477091	39.12651402293	2.1343	−10.799	−10.518	9.80
4648485	TNG	2 101 044 507 393 877 248	289.8882549336	39.76055768539	2.2062	3.844	−5.397	10.53
4756219	TNG	2 076 460 526 911 309 440	294.40519631193	39.80229068803	1.1785	14.91	25.146	11.00
4826087	NOT	2 101 241 629 211 118 720	288.91716240894	39.96424275903	1.7006	−9.6	−9.419	9.51
4913049	TNG	2 101 299 211 835 208 704	288.49796516747	40.08652722798	2.9383	4.729	12.322	10.30
4931389	TNG	2 052 513 438 539 100 544	293.90812945332	40.07863655336	3.3937	5.606	19.098	9.68
5265256	TNG	2 101 334 224 404 935 808	288.78444311507	40.49287806719	1.3298	−5.758	−24.946	10.62
5769244	TNG	2 103 697 147 912 507 904	283.41902409105	41.03654428312	2.9417	−25.193	−24.086	9.86
5882005	NOT	2 077 382 948 448 694 144	293.58754916997	41.10299865842	1.7129	−6.663	−26.876	10.19
5940060	TNG	2 103 703 160 866 757 376	283.84136373493	41.23187541068	2.0936	−6.442	−29.312	9.68
6365511	TNG	2 101 681 880 540 210 816	292.29333546278	41.78788591373	1.1798	−1.29	−25.558	11.25
6547007	TNG	2 075 411 524 106 352 896	298.23841960779	41.97024284079	1.2814	8.739	−4.842	10.45
6851499	TNG	2 102 506 548 618 822 272	288.09390243154	42.39708323493	1.2974	−8.761	−23.784	10.66
6859803	NOT	2 101 942 288 694 401 792	290.80359448096	42.33279512806	2.7956	25.759	41.3	9.81
6964342	NOT	2 077 220 426 885 950 976	296.0893851256	42.43766636329	1.667	14.996	29.675	9.84
7429055	TNG	2 105 552 608 144 587 008	286.30448783205	43.03668783654	1.1228	−7.816	9.118	11.19
7430868	TNG	2 105 587 513 340 280 832	287.07512031919	43.00396515398	1.6869	−12.007	1.624	10.22
7450230	TNG	2 077 839 520 649 382 912	293.39148078301	43.03586846178	5.0844	−16.225	−30.856	9.06
7533995	TNG	2 078 201 569 212 490 112	293.63876550384	43.10556031286	2.3541	−14.546	−13.262	10.11
7617227	TNG	2 077 985 893 136 622 720	294.65772917773	43.2050581937	2.246	7.274	28.134	9.62
7812552	TNG	2 102 960 333 383 028 864	288.21198411368	43.50628926117	3.0691	2.044	−10.235	10.09
8129047	TNG	2 076 056 903 066 401 408	300.79512348024	43.98263371667	1.4667	3.739	10.518	10.70
8493969	TNG	2 126 240 056 861 504 768	291.31898259395	44.52162539813	1.8747	−18.969	−1.276	10.59
8587329	TNG	2 076 151 186 191 153 408	300.15781414731	44.65790976271	1.901	−4.434	−21.296	10.38
8590920	TNG	2 082 106 038 083 789 184	301.2334322159	44.66624917466	1.3475	−2.408	−10.732	11.01
8612241	NOT	2 106 313 740 768 003 712	286.26347122477	44.70791149712	1.3996	6.049	−22.101	10.24
8737032	NOT	2 106 790 314 639 185 280	283.86388902736	44.98524940721	1.2746	6.929	9.98	10.19
9080175	TNG	2 130 239 221 168 800 128	288.03397469718	45.49335362678	1.6128	−6.065	−8.657	10.15
9145955	NOT	2 130 219 769 257 640 576	287.8855801582	45.52287564413	2.4141	3.138	−15.988	9.77
9535399	TNG, NOT	2 080 029 640 428 099 840	295.3782447566	46.15220017926	2.2502	7.537	−9.335	9.63
9640480	TNG	2 130 416 929 734 202 624	287.71772206553	46.39464244871	1.4604	−9.38	9.414	10.70
9711269	TNG, NOT	2 128 306 485 885 973 248	292.24848338049	46.41193805565	2.138	0.928	25.083	9.77
9772366	TNG	2 128 291 127 083 154 432	292.59732866502	46.58594066557	1.9758	4.309	−13.709	9.66
9777293	TNG	2 128 141 627 862 366 720	294.54782801418	46.59345892176	1.9066	−9.328	9.874	10.99
9783226	NOT	2 080 331 907 350 333 312	296.68965799804	46.58398730699	1.6824	0.844	11.227	9.84
9967700	TNG	2 086 305 725 822 665 728	297.91512418488	46.87070339907	1.9044	−5.736	5.194	10.30
10095427	TNG	2 085 570 771 021 453 056	298.69412782257	47.08869166931	2.2811	8.92	−47.646	9.61
10351820	NOT	2 080 579 160 028 012 928	296.33947586705	47.41981620496	1.7124	11.351	−2.045	9.86
10513837	NOT	2 119 801 557 282 726 912	280.86796292697	47.70362889589	3.7792	4.718	−1.304	9.21
10550429	TNG	2 086 419 800 156 327 680	297.34535863072	47.78287096973	2.556	−5.297	−25.731	9.57
10659842	NOT	2 127 945 639 913 049 984	289.44254327873	47.94136786497	1.7343	10.002	13.189	9.90
10722175	NOT	2 130 984 827 490 239 232	288.09718661588	48.06239066917	2.8962	2.505	28.877	9.46
10793771	NOT	2 129 414 106 412 064 256	290.4112575946	48.1503155865	1.2973	−0.953	−17.183	10.25
10801063	TNG	2 128 852 943 165 070 336	293.40401419551	48.12821469224	2.6771	−28.996	−32.222	10.37
10992711	TNG	2 086 863 212 577 271 040	298.79955322383	48.40574133545	1.6143	13.523	40.395	9.95
11020211	TNG	2 131 166 276 968 591 360	286.72887458747	48.50281492322	1.9772	−37.815	59.779	10.41
11029423	TNG	2 129 338 961 663 941 504	291.71024475923	48.59500213454	2.7315	−9.554	21.707	9.46
11087371	TNG, NOT	2 129 006 870 493 887 744	293.46990960596	48.61222842243	2.8327	−7.734	−1.006	9.76
11228549	TNG	2 143 769 635 160 629 760	282.56542385642	48.90544475372	1.1368	−3.458	4.498	10.95
11250139	TNG	2 134 800 338 999 043 584	294.63588634634	48.95780220302	1.1997	6.304	−17.961	10.69
11358669	NOT	2 134 772 129 653 795 328	295.7471194045	49.19190636441	2.1599	21.089	29.626	9.74
11453721	TNG	2 129 947 988 025 131 520	291.02538198849	49.38136639365	1.9252	0.654	−26.499	9.94
11496569	NOT	2 132 105 435 996 154 368	285.71381737169	49.49053613947	1.8927	−12.441	−10.541	9.55
11550492	TNG	2 131 326 599 508 772 352	286.74955720864	49.54020004945	3.1245	−4.51	19.454	9.26

Table 1 – *continued*

Name (KIC)	Telescope	*Gaia* DR3 ID	RA (J2000)	Dec.	Plx (mas)	μ_α (mas yr^{-1})	μ_δ (mas yr^{-1})	Gmag
11702195	TNG	2 132 142 166 556 843 264	285.6532396511	49.81256772245	1.3476	5.714	18.753	10.63
11775511	TNG	2 087 252 680 210 082 432	297.52129742582	49.97923069817	1.519	−3.225	−11.811	10.33
11819363	NOT	2 135 151 083 206 715 008	294.55092213007	50.08866204207	2.0492	−9.251	−4.202	9.39
12115227	TNG	2 135 229 973 166 427 008	293.99161760649	50.63598157364	2.3219	−13.407	6.422	9.95
12122151	NOT	2 135 411 834 961 721 728	297.08500386861	50.60769726425	1.6858	0.516	−7.605	9.69
12647227	TNG, NOT	2 139 238 517 681 314 944	290.55928721926	51.78082445724	1.7849	4.43	−1.281	9.41

where log $g_\odot = 4.44$ dex, $\nu_{\max,\odot} = 3090\ \mu$Hz, and $T_{\rm eff,\odot} = 5777$ K (Huber et al. 2011; Handberg et al. 2017). The evaluation of the uncertainties on the final atmospheric parameters is described by Magrini et al. (2013). Finally, the elemental abundances computed by FAMA are: Na, Mg, Al, Si, Ca, Sc, Ti (I and II), V, Cr (I and II), Mn, Fe (I and II), Co, Ni, Cu, Zn, Sr, Y, Zr (I and II), Ba, La, Ce, Pr, Nd, Sm, and Eu (the *n*-capture elements are not available in the APOGEE survey for these stars, except Ce – for this reason, we observed stars with previously measured APOGEE abundances using spectrographs that include the blue spectral region, which contains key absorption lines of neutron-capture elements). The Solar abundance scale adopted in this work is from Asplund et al. (2009). When only one line is detected, as is the case for Ba, the observational error is estimated through the uncertainty on the EW measured by DOOp. No systematic offsets were found between the FIES and HARPS-N spectra for the four stars observed by both instruments, for this reason we use the average of the two values. In Tables 2 and 3, we present the results of our spectral analysis.[2]

2.2 Comparison with APOGEE DR17

The atmospheric parameters and some abundances are available in APOGEE DR17 for our sample of stars. We compared our atmospheric parameters and [α/Fe] with those available in APOGEE DR17. As we can see from Fig. 1, $T_{\rm eff}$ and [Fe/H] are in good agreement, without any systematic trend, but with an offset: our temperatures $T_{\rm eff}$ are on average higher by ~ 45 K and our metallicities are on average lower by ~ 0.05 dex than those of APOGEE (similar offset are found by Hegedűs et al. (2023) among APOGEE and the optical surveys Galactic Archaeology with HERMES, GALAH (De Silva et al. 2015), and *Gaia*-ESO). The seismic log g is in agreement with the log g of APOGEE, which is calibrated on a set of surface gravities from asteroseismology and isochrones using *Kepler* stars (Abdurro'uf et al. 2022). Finally, [α/Fe] shows an average offset of 0.05 dex. The [α/Fe] ratio is computed as 1/4([Ca/Fe] + [Mg/Fe] + [Si/Fe] + [Ti/Fe]) in both cases.

Fig. 2 shows the comparison between all the abundances in common with the APOGEE survey. The agreement is poor for Na, Si, V, and Ce, whereas it is good for the other elements. APOGEE spectra contain two weak lines of sodium, close to telluric lines (Barbuy et al. 2023). Therefore, sodium is one of the least precisely determined element abundances in the APOGEE survey. Although Si is considered one of the most precisely measured elements in APOGEE, there is a large offset between our measurements and the APOGEE ones (offset of the order of 0.1 dex). This offset is related to the solar Si abundance reported by Asplund et al. (2009).

[2]In this work, we present the abundances of elements used in our analysis and compared with the APOGEE survey: Na, Mg, Al, Si, Ca, Ti (I and II), V, Cr, Fe (I and II), Co, Ni, Y, Zr I, Ba, La, and Ce.

Table 2. Atmospheric parameters derived from spectral analysis, along with log g obtained from asteroseismology, for the *Kepler* stars.

Name	$T_{\rm eff}$ (K)	log$g$ (seismo) (dex)	[Fe/H] (dex)	ξ (dex)
1433803	4683 ± 89	3.079 ± 0.004	0.14 ± 0.01	1.40 ± 0.07
2451509	4942 ± 76	2.820 ± 0.004	−0.15 ± 0.04	1.49 ± 0.07
2970584	4694 ± 109	2.698 ± 0.005	−0.33 ± 0.03	1.36 ± 0.09
3429738	4664 ± 119	2.651 ± 0.005	−0.41 ± 0.03	1.33 ± 0.08
3539408	5002 ± 110	2.971 ± 0.004	−0.23 ± 0.05	1.18 ± 0.09
3644223	4958 ± 80	3.127 ± 0.003	−0.21 ± 0.03	1.29 ± 0.09
3661494	4903 ± 90	2.852 ± 0.003	−0.38 ± 0.04	1.14 ± 0.08
3744043	5023 ± 100	2.960 ± 0.003	−0.36 ± 0.05	1.18 ± 0.08
4055294	5021 ± 94	2.989 ± 0.004	0.17 ± 0.03	1.45 ± 0.08
4648485	4754 ± 110	3.056 ± 0.003	−0.08 ± 0.02	1.16 ± 0.10
4756219	4597 ± 142	2.602 ± 0.010	−0.25 ± 0.01	1.29 ± 0.11
4826087	4802 ± 94	2.559 ± 0.010	−0.10 ± 0.04	1.53 ± 0.07
4913049	4944 ± 136	3.246 ± 0.003	−0.07 ± 0.04	0.99 ± 0.12
4931389	5007 ± 107	3.218 ± 0.004	0.11 ± 0.03	1.07 ± 0.10
5265256	4639 ± 120	2.619 ± 0.005	−0.26 ± 0.02	1.34 ± 0.10
5769244	4756 ± 106	3.046 ± 0.003	0.08 ± 0.02	1.01 ± 0.09
5882005	4843 ± 70	2.818 ± 0.004	−0.16 ± 0.03	1.34 ± 0.06
5940060	4683 ± 93	2.615 ± 0.008	−0.45 ± 0.04	1.32 ± 0.07
6365511	4845 ± 74	2.789 ± 0.003	−0.62 ± 0.04	1.31 ± 0.07
6547007	4772 ± 103	2.475 ± 0.005	−0.82 ± 0.06	1.44 ± 0.08
6851499	4671 ± 110	2.612 ± 0.006	−0.39 ± 0.03	1.31 ± 0.08
6859803	5059 ± 104	3.146 ± 0.003	−0.17 ± 0.04	1.18 ± 0.08
6964342	4604 ± 88	2.507 ± 0.011	−0.09 ± 0.02	1.55 ± 0.07
7429055	4550 ± 84	2.669 ± 0.006	−0.09 ± 0.02	1.20 ± 0.05
7430868	4567 ± 89	2.627 ± 0.006	−0.34 ± 0.02	1.24 ± 0.07
7450230	4909 ± 122	3.238 ± 0.003	−0.13 ± 0.03	0.99 ± 0.12
7533995	4656 ± 76	2.929 ± 0.003	−0.08 ± 0.03	1.12 ± 0.04
7617227	4866 ± 117	2.780 ± 0.004	−0.33 ± 0.04	1.18 ± 0.11
7812552	5106 ± 76	3.235 ± 0.003	−0.52 ± 0.04	1.06 ± 0.05
8129047	4635 ± 69	2.682 ± 0.004	−0.08 ± 0.02	1.10 ± 0.05
8493969	4830 ± 91	2.942 ± 0.003	−0.34 ± 0.04	1.07 ± 0.06
8587329	4357 ± 111	2.718 ± 0.005	0.14 ± 0.00	1.13 ± 0.09
8590920	4460 ± 77	2.785 ± 0.006	0.18 ± 0.05	1.26 ± 0.05
8612241	5029 ± 103	2.811 ± 0.005	−0.23 ± 0.06	1.53 ± 0.07
8737032	4711 ± 71	2.535 ± 0.004	−0.21 ± 0.02	1.54 ± 0.08
9080175	4700 ± 106	2.586 ± 0.005	−0.55 ± 0.04	1.33 ± 0.09
9145955	5064 ± 95	3.027 ± 0.004	−0.30 ± 0.04	1.32 ± 0.09
9535399	4549 ± 62	2.653 ± 0.005	0.12 ± 0.02	1.08 ± 0.03
9640480	4764 ± 75	2.581 ± 0.004	−0.40 ± 0.02	1.17 ± 0.09
9711269	4656 ± 119	2.709 ± 0.004	0.07 ± 0.02	1.09 ± 0.07
9772366	4691 ± 105	2.780 ± 0.005	0.14 ± 0.02	1.11 ± 0.08
9777293	5006 ± 73	3.171 ± 0.003	−0.61 ± 0.04	1.23 ± 0.06
9783226	4762 ± 75	2.625 ± 0.003	−0.02 ± 0.03	1.38 ± 0.07
9967700	4976 ± 76	2.944 ± 0.003	−0.42 ± 0.04	1.15 ± 0.07
10095427	4682 ± 103	2.662 ± 0.004	−0.55 ± 0.04	1.26 ± 0.08
10351820	4788 ± 77	2.658 ± 0.006	−0.12 ± 0.03	1.40 ± 0.08
10513837	5024 ± 112	3.199 ± 0.003	0.04 ± 0.04	1.31 ± 0.08
10550429	4980 ± 118	3.030 ± 0.004	0.02 ± 0.04	1.06 ± 0.10
10659842	4973 ± 79	2.784 ± 0.004	−0.22 ± 0.04	1.32 ± 0.08
10722175	4764 ± 86	2.957 ± 0.003	0.11 ± 0.03	1.39 ± 0.07

Table 2 – *continued*

Name	$T_{\rm eff}$ (K)	log*g* (seismo) (dex)	[Fe/H] (dex)	ξ (dex)
10793771	4956 ± 105	2.806 ± 0.003	0.05 ± 0.04	1.48 ± 0.09
10801063	4948 ± 80	3.207 ± 0.002	-0.35 ± 0.03	0.95 ± 0.06
10992711	4571 ± 119	2.444 ± 0.004	-0.44 ± 0.03	1.38 ± 0.10
11020211	4891 ± 83	2.937 ± 0.003	-0.40 ± 0.03	1.07 ± 0.07
11029423	4616 ± 116	2.779 ± 0.004	-0.16 ± 0.02	1.21 ± 0.08
11087371	4739 ± 72	3.056 ± 0.004	0.14 ± 0.02	1.07 ± 0.05
11228549	4890 ± 89	2.649 ± 0.004	-0.83 ± 0.05	1.42 ± 0.08
11250139	4675 ± 98	2.506 ± 0.005	-0.53 ± 0.04	1.35 ± 0.07
11358669	4899 ± 61	2.896 ± 0.003	0.11 ± 0.02	1.41 ± 0.07
11453721	4615 ± 107	2.685 ± 0.003	-0.42 ± 0.04	1.25 ± 0.09
11496569	4894 ± 117	2.730 ± 0.003	-0.03 ± 0.05	1.46 ± 0.09
11550492	4801 ± 86	2.875 ± 0.003	-0.07 ± 0.03	1.03 ± 0.08
11702195	4662 ± 97	2.619 ± 0.005	-0.51 ± 0.04	1.29 ± 0.07
11775511	4756 ± 73	2.574 ± 0.004	-0.32 ± 0.03	1.20 ± 0.07
11819363	4868 ± 84	2.611 ± 0.005	-0.37 ± 0.04	1.33 ± 0.10
12115227	4903 ± 78	2.898 ± 0.003	-0.77 ± 0.04	1.32 ± 0.08
12122151	4739 ± 122	2.610 ± 0.008	-0.15 ± 0.04	1.52 ± 0.10
12647227	4803 ± 96	2.491 ± 0.007	-0.54 ± 0.05	1.29 ± 0.09

To investigate further, we analysed a solar spectrum collected with the HARPS spectrograph and we found excellent agreement with the Asplund et al. (2009) values for all elements in common (differences < 0.03 dex), except for silicon, where we found a difference of 0.07 dex ($A(Si)_{\odot} = 7.44$). By adopting this updated solar Si abundance, the offset with APOGEE measurements can be reduced to 0.06 dex. Vanadium abundances (0.3 dex of offset) have rather low precision in APOGEE and they should be used with caution (Jönsson et al. 2020; Hegedűs et al. 2023). Finally, Ce in APOGEE DR17 (Cunha et al. 2017; Sales-Silva et al. 2022, 2024) is lower by a factor of 0.1 dex with respect to the abundances shown in this work, with a larger scatter at lower metallicity (Hayes et al. (2022) found a metallicity-correlated offset for Ce at [Fe/H] < -1 dex, which lies outside the metallicity range considered in this work). This trend is already seen when the Ce of APOGEE is compared with the Ce from the optical survey *Gaia*-ESO (Casali et al. 2023).

2.3 Age from asteroseismology

The 4.5-yr long *Kepler* light curves provide high-quality oscillation data, allowing for precise identification and characterization of oscillation modes. The sample of stars, chosen from seismically classified RGBs in the *Kepler* field, was also manually inspected to ensure that any other potential signals in the light curve did not affect the extraction and characterization of oscillation modes. Indeed, the presence of overlapping solar-like oscillation signals in the power spectral density, as well as harmonics from other classical pulsators in the field or signals due to stellar rotation, can interfere with the accurate identification of both oscillation modes and background components. Seventy-five per cent of the targets have seven or more identified radial modes. The frequencies of these modes, along with the frequency at maximum power ($\nu_{\rm max}$) and, when available, the asymptotic period spacing (referred to the regular spacing in period between gravity modes and derived from mixed dipolar modes by Vrard, Mosser & Samadi 2016), are used as seismic observational constraints in the process of determining stellar parameters. For this purpose, we used the AIMS code (Reese 2016; Rendle et al. 2019), which implements a Bayesian inference approach to provide posterior probability distributions for the stellar parameters. Additional 'classical' observational data included in the process are the effective temperature and the current metal abundance ([M/H]) in the photospheres of these stars. Given the constraints provided by asteroseismic frequencies, and the overall agreement of our stellar parameters with those in APOGEE shown in Section 2.2, the impact of adopting one or the other set of 'classical' stellar parameters is limited. For consistency with the more extensive catalogue of *Kepler* stars that will be presented in Montalbán et al. (in preparation), we have adopted effective temperature, [α/M], and [M/H] from APOGEE-DR17. Thomsen et al. (2025) show that adopting different spectroscopic input values in the AIMS code does not significantly affect the inferred stellar ages. In their table G.2, they report a difference of only 0.25σ between the ages computed using atmospheric parameters from APOGEE and those derived from spectra collected with FIES and analysed in the same way as presented in this work.[3]

Compared to the work presented in Montalbán et al. (2021), which focused on a low-metallicity sample, we have extended the range of chemical composition in the grid of models at the base of the method. In this study, we have adopted a grid computed with a helium enrichment law of $\Delta Y/\Delta Z = 1.5$, as adopted in several studies (e.g. Brogaard et al. 2012; Miglio et al. 2021) and consistent with measurements (e.g. Casagrande et al. 2007; Verma et al. 2019). For details on the impact of $\Delta Y/\Delta Z$ on the determination of stellar parameters, see Montalbán et al. (in preparation).

As will be shown in Montalbán et al. (in preparation), using individual frequencies as observational constraints instead of global seismic parameters allows us to reduce the internal uncertainty in estimating stellar ages. In the sample analysed in this paper, 50 per cent of the targets have an age uncertainty between 7 per cent and 9 per cent estimated using individual mode frequencies (see Fig. 3). This is lower than the typical value of 20–23 per cent reported in Miglio et al. (2021), which was estimated using the Bayesian code PARAM (da Silva et al. 2006; Rodrigues et al. 2017) with global seismic parameters, APOGEE-DR14, and *Gaia*-DR2 data as constraints. A recent update (Willett et al., submitted) using APOGEE-DR17 and *Gaia*-DR3 has further decreased the typical age uncertainty with that method. As a result, 50 per cent of the stars in our sample have age values estimated by PARAM using global seismic parameters with an uncertainty between 10 per cent and 14.25 per cent.

The mean difference between ages derived with both methods, normalized by their uncertainties $(\tau_{\rm PARAM} - \tau_{\rm AIMS})/\left(\sqrt{\sigma^2_{\rm PARAM} + \sigma^2_{\rm AIMS}}\right)$ is -0.72. Indeed, PARAM ages tend to be smaller than AIMS ones as we can see from Fig. 4. For half of the sample, this difference falls between -1.2 and 0.07.

Recently, Pinsonneault et al. (2025) estimated a median fractional age uncertainty of ~ 11.1 per cent for their gold sample of the third release of the APOGEE-*Kepler* Asteroseismic Science Consortium (APOKASC-3) catalogue using global seismic parameters (comparisons of APOKASC-3 against APO-K2 sample, a combination of spectroscopic observations with APOGEE survey and asteroseismic data from the K2 mission, are lately present in Schonhut-Stasik et al. 2024; Warfield et al. 2024). However, we found that APOKASC-3 yields younger ages compared to those computed via individual mode frequencies, with an average offset of 0.9 Gyr, increasing to up

[3]The differences in $T_{\rm eff}$ and [Fe/H] between the two spectral analyses are 25 K and 0.05 dex, respectively. The APOGEE uncertainties were inflated to 60 K and 0.05 dex in the calculation as they are systematically underestimated in the survey, compared to the FIES uncertainties of 36 K and 0.07 dex.

Table 3. Chemical abundances for the sample of *Kepler* stars.

Name	Na/H	Mg/H	Al/H	Si/H	Ca/H	TiI/H	TiII/H	V/H	Cr/H
1433803	6.70 ± 0.03	7.97 ± 0.11	6.75 ± 0.10	7.72 ± 0.07	6.43 ± 0.14	5.11 ± 0.09	5.15 ± 0.20	4.34 ± 0.08	5.83 ± 0.10
2451509	6.26 ± 0.07	7.56 ± 0.06	6.36 ± 0.06	7.35 ± 0.03	6.23 ± 0.07	4.92 ± 0.07	4.85 ± 0.10	4.01 ± 0.11	5.58 ± 0.04
2970584	6.23 ± 0.08	7.59 ± 0.20	6.54 ± 0.02	7.26 ± 0.01	6.24 ± 0.08	5.00 ± 0.07	4.86 ± 0.11	4.09 ± 0.08	5.47 ± 0.06
3429738	6.10 ± 0.06	7.62 ± 0.01	6.40 ± 0.12	7.26 ± 0.01	6.10 ± 0.07	4.83 ± 0.06	4.83 ± 0.08	3.92 ± 0.09	5.31 ± 0.06
3539408	6.12 ± 0.04	7.47 ± 0.02	6.21 ± 0.01	7.21 ± 0.02	6.14 ± 0.04	4.80 ± 0.05	4.82 ± 0.07	3.83 ± 0.08	5.41 ± 0.05
3644223	6.21 ± 0.10	7.57 ± 0.08	6.33 ± 0.04	7.35 ± 0.02	6.13 ± 0.04	4.83 ± 0.06	4.87 ± 0.12	3.88 ± 0.11	5.49 ± 0.07
3661494	5.96 ± 0.04	7.40 ± 0.02	6.23 ± 0.04	7.12 ± 0.01	6.03 ± 0.03	4.72 ± 0.06	4.75 ± 0.07	3.74 ± 0.09	5.25 ± 0.05
3744043	5.98 ± 0.05	7.29 ± 0.03	6.14 ± 0.07	7.10 ± 0.01	6.00 ± 0.05	4.72 ± 0.06	4.68 ± 0.07	3.73 ± 0.08	5.28 ± 0.04
4055294	6.79 ± 0.06	7.95 ± 0.07	6.80 ± 0.04	7.62 ± 0.03	6.55 ± 0.12	5.30 ± 0.09	5.11 ± 0.17	4.51 ± 0.09	5.92 ± 0.07
4648485	6.34 ± 0.07	7.78 ± 0.01	6.61 ± 0.06	7.47 ± 0.02	6.33 ± 0.04	5.03 ± 0.06	5.08 ± 0.13	4.18 ± 0.09	5.64 ± 0.06
4756219	6.20 ± 0.07	7.66 ± 0.02	6.48 ± 0.04	7.30 ± 0.01	6.18 ± 0.04	4.85 ± 0.06	4.88 ± 0.13	3.97 ± 0.08	5.47 ± 0.06
4826087	6.38 ± 0.08	7.73 ± 0.11	6.47 ± 0.01	7.40 ± 0.05	6.36 ± 0.10	5.00 ± 0.07	4.90 ± 0.12	4.12 ± 0.07	5.66 ± 0.07
4913049	6.35 ± 0.08	7.85 ± 0.05	6.65 ± 0.05	7.34 ± 0.01	6.37 ± 0.07	5.18 ± 0.07	5.07 ± 0.11	4.38 ± 0.12	5.68 ± 0.07
4931389	6.57 ± 0.05	7.80 ± 0.02	6.62 ± 0.10	7.44 ± 0.03	6.45 ± 0.03	5.21 ± 0.07	5.07 ± 0.14	4.47 ± 0.11	5.84 ± 0.07
5265256	6.12 ± 0.06	7.62 ± 0.04	6.42 ± 0.01	7.28 ± 0.02	6.16 ± 0.03	4.82 ± 0.06	4.85 ± 0.10	3.93 ± 0.08	5.47 ± 0.05
5769244	6.54 ± 0.06	7.96 ± 0.04	6.74 ± 0.07	7.48 ± 0.03	6.47 ± 0.04	5.21 ± 0.08	5.16 ± 0.17	4.40 ± 0.10	5.83 ± 0.08
5882005	6.23 ± 0.08	7.62 ± 0.05	6.41 ± 0.03	7.42 ± 0.03	6.20 ± 0.07	4.88 ± 0.07	4.90 ± 0.12	3.98 ± 0.11	5.50 ± 0.07
5940060	6.08 ± 0.05	7.59 ± 0.01	6.33 ± 0.17	7.21 ± 0.01	6.05 ± 0.07	4.84 ± 0.06	4.77 ± 0.09	3.90 ± 0.08	5.29 ± 0.06
6365511	5.85 ± 0.06	7.34 ± 0.11	6.20 ± 0.03	7.06 ± 0.01	5.92 ± 0.03	4.65 ± 0.06	4.64 ± 0.07	3.62 ± 0.06	5.08 ± 0.04
6547007	5.60 ± 0.03	7.24 ± 0.04	5.96 ± 0.10	6.95 ± 0.01	5.68 ± 0.04	4.35 ± 0.05	4.47 ± 0.05	3.29 ± 0.06	4.81 ± 0.05
6851499	6.06 ± 0.08	7.62 ± 0.01	6.37 ± 0.04	7.21 ± 0.02	6.05 ± 0.06	4.76 ± 0.06	4.80 ± 0.09	3.85 ± 0.09	5.32 ± 0.06
6859803	6.24 ± 0.12	7.57 ± 0.09	6.31 ± 0.03	7.38 ± 0.02	6.21 ± 0.09	4.90 ± 0.08	4.93 ± 0.09	3.95 ± 0.15	5.44 ± 0.08
6964342	6.52 ± 0.07	7.79 ± 0.09	6.60 ± 0.08	7.47 ± 0.01	6.37 ± 0.10	5.01 ± 0.08	4.89 ± 0.16	4.19 ± 0.09	5.75 ± 0.08
7429055	6.43 ± 0.08	7.83 ± 0.04	6.69 ± 0.07	7.41 ± 0.01	6.35 ± 0.04	5.04 ± 0.07	5.08 ± 0.15	4.21 ± 0.07	5.63 ± 0.06
7430868	6.17 ± 0.06	7.69 ± 0.02	6.20 ± 0.10	7.30 ± 0.01	6.15 ± 0.06	4.86 ± 0.06	4.92 ± 0.11	3.95 ± 0.08	5.38 ± 0.07
7450230	6.27 ± 0.09	7.71 ± 0.04	6.54 ± 0.04	7.31 ± 0.01	6.28 ± 0.04	5.05 ± 0.06	5.03 ± 0.11	4.22 ± 0.11	5.59 ± 0.06
7533995	6.37 ± 0.06	7.83 ± 0.03	6.66 ± 0.06	7.43 ± 0.01	6.33 ± 0.04	5.04 ± 0.06	5.08 ± 0.14	4.22 ± 0.08	5.63 ± 0.07
7617227	6.07 ± 0.05	7.42 ± 0.04	6.25 ± 0.04	7.14 ± 0.03	6.03 ± 0.02	4.69 ± 0.05	4.74 ± 0.08	3.75 ± 0.08	5.31 ± 0.05
7812552	5.97 ± 0.06	7.52 ± 0.10	6.14 ± 0.01	7.05 ± 0.02	6.01 ± 0.02	4.75 ± 0.05	4.71 ± 0.05	3.66 ± 0.07	5.16 ± 0.05
8129047	6.44 ± 0.05	7.82 ± 0.01	6.67 ± 0.04	7.40 ± 0.03	6.41 ± 0.06	5.17 ± 0.07	5.07 ± 0.17	4.35 ± 0.10	5.71 ± 0.07
8493969	6.13 ± 0.06	7.62 ± 0.02	6.46 ± 0.01	7.24 ± 0.02	6.18 ± 0.04	4.91 ± 0.06	4.88 ± 0.09	3.98 ± 0.10	5.36 ± 0.05
8587329	6.59 ± 0.10	7.99 ± 0.02	6.79 ± 0.07	7.68 ± 0.02	6.47 ± 0.23	5.01 ± 0.07	5.35 ± 0.22	4.26 ± 0.07	5.78 ± 0.08
8590920	6.67 ± 0.06	8.03 ± 0.03	6.73 ± 0.07	7.71 ± 0.03	6.55 ± 0.06	5.13 ± 0.08	5.34 ± 0.24	4.43 ± 0.06	5.89 ± 0.08
8612 241	6.28 ± 0.08	7.62 ± 0.10	6.33 ± 0.04	7.35 ± 0.06	6.17 ± 0.08	4.89 ± 0.07	4.79 ± 0.09	3.96 ± 0.12	5.50 ± 0.06
8737032	6.23 ± 0.01	7.63 ± 0.08	6.41 ± 0.01	7.36 ± 0.02	6.18 ± 0.07	4.83 ± 0.07	4.83 ± 0.10	3.93 ± 0.08	5.50 ± 0.06
9080175	5.98 ± 0.04	7.53 ± 0.02	6.33 ± 0.04	7.14 ± 0.01	5.99 ± 0.07	4.75 ± 0.06	4.71 ± 0.08	3.79 ± 0.09	5.19 ± 0.05
9145955	6.10 ± 0.06	7.58 ± 0.14	6.24 ± 0.01	7.22 ± 0.06	6.12 ± 0.06	4.79 ± 0.07	4.80 ± 0.07	3.81 ± 0.13	5.38 ± 0.05
9535399	6.67 ± 0.12	7.77 ± 0.19	6.78 ± 0.08	7.57 ± 0.06	6.49 ± 0.06	5.20 ± 0.08	5.24 ± 0.19	4.44 ± 0.07	5.86 ± 0.07
9640480	6.09 ± 0.04	7.58 ± 0.01	6.32 ± 0.20	7.19 ± 0.01	6.14 ± 0.04	4.89 ± 0.06	4.78 ± 0.09	3.98 ± 0.10	5.31 ± 0.06
9711269	6.53 ± 0.07	7.83 ± 0.02	6.67 ± 0.16	7.45 ± 0.01	6.48 ± 0.06	5.19 ± 0.08	5.09 ± 0.18	4.41 ± 0.08	5.84 ± 0.07
9772366	6.84 ± 0.10	7.89 ± 0.04	6.73 ± 0.12	7.54 ± 0.02	6.51 ± 0.06	5.24 ± 0.08	5.15 ± 0.17	4.46 ± 0.08	5.90 ± 0.06
9777293	5.79 ± 0.04	7.46 ± 0.01	–	7.00 ± 0.05	5.95 ± 0.05	4.70 ± 0.06	4.66 ± 0.06	3.61 ± 0.07	5.09 ± 0.04
9783226	6.54 ± 0.08	7.75 ± 0.08	6.60 ± 0.01	7.44 ± 0.08	6.38 ± 0.06	5.03 ± 0.08	5.00 ± 0.14	4.21 ± 0.10	5.69 ± 0.06
9967700	5.94 ± 0.06	7.38 ± 0.02	6.08 ± 0.01	7.13 ± 0.01	5.99 ± 0.04	4.67 ± 0.05	4.68 ± 0.07	3.67 ± 0.09	5.22 ± 0.05
10095427	5.99 ± 0.05	7.56 ± 0.04	6.23 ± 0.18	7.19 ± 0.01	6.03 ± 0.06	4.76 ± 0.06	4.82 ± 0.07	3.80 ± 0.09	5.16 ± 0.05
10351820	6.40 ± 0.09	7.66 ± 0.08	6.46 ± 0.02	7.42 ± 0.07	6.34 ± 0.07	4.93 ± 0.08	4.93 ± 0.17	4.09 ± 0.09	5.59 ± 0.07
10513837	6.50 ± 0.08	7.79 ± 0.07	6.57 ± 0.01	7.49 ± 0.06	6.46 ± 0.07	5.10 ± 0.08	5.02 ± 0.16	4.24 ± 0.11	5.75 ± 0.08
10550429	6.47 ± 0.06	7.58 ± 0.14	6.55 ± 0.07	7.36 ± 0.01	6.38 ± 0.04	5.09 ± 0.07	4.97 ± 0.13	4.31 ± 0.12	5.71 ± 0.05
10659842	6.18 ± 0.12	7.60 ± 0.09	–	7.25 ± 0.03	6.18 ± 0.09	4.85 ± 0.07	4.90 ± 0.10	3.88 ± 0.09	5.45 ± 0.06
10722175	6.74 ± 0.06	7.88 ± 0.08	6.72 ± 0.11	7.69 ± 0.14	6.44 ± 0.11	5.16 ± 0.09	5.18 ± 0.21	4.35 ± 0.09	5.84 ± 0.08
10793771	6.52 ± 0.09	7.85 ± 0.09	6.62 ± 0.01	7.46 ± 0.04	6.46 ± 0.08	5.10 ± 0.08	4.93 ± 0.12	4.25 ± 0.10	5.77 ± 0.08
10801063	6.08 ± 0.05	7.70 ± 0.07	6.31 ± 0.17	7.22 ± 0.01	6.17 ± 0.04	4.94 ± 0.05	4.92 ± 0.08	3.96 ± 0.10	5.34 ± 0.05
10992711	6.10 ± 0.05	7.62 ± 0.02	6.30 ± 0.27	7.24 ± 0.01	6.08 ± 0.07	4.82 ± 0.06	4.79 ± 0.09	3.88 ± 0.07	5.30 ± 0.06
11020211	6.01 ± 0.05	7.54 ± 0.01	6.33 ± 0.02	7.16 ± 0.01	6.09 ± 0.04	4.84 ± 0.05	4.79 ± 0.08	3.84 ± 0.08	5.26 ± 0.05
11029423	6.30 ± 0.08	7.74 ± 0.01	6.59 ± 0.06	7.43 ± 0.01	6.26 ± 0.05	4.96 ± 0.07	4.99 ± 0.13	4.09 ± 0.07	5.57 ± 0.07
11087371	6.72 ± 0.06	7.92 ± 0.01	6.73 ± 0.12	7.57 ± 0.01	6.49 ± 0.06	5.19 ± 0.08	5.17 ± 0.17	4.46 ± 0.09	5.87 ± 0.08
11228549	5.63 ± 0.04	7.19 ± 0.07	6.01 ± 0.01	6.88 ± 0.01	5.72 ± 0.03	4.45 ± 0.06	4.46 ± 0.05	3.35 ± 0.06	4.82 ± 0.04
11250139	5.97 ± 0.05	7.47 ± 0.04	6.22 ± 0.14	7.16 ± 0.02	5.98 ± 0.06	4.72 ± 0.06	4.73 ± 0.08	3.77 ± 0.09	5.18 ± 0.06
11358669	6.66 ± 0.01	7.89 ± 0.07	6.71 ± 0.07	7.57 ± 0.04	6.58 ± 0.07	5.25 ± 0.08	5.05 ± 0.14	4.45 ± 0.09	5.90 ± 0.06
11453721	6.11 ± 0.06	7.66 ± 0.06	6.38 ± 0.05	7.26 ± 0.01	6.02 ± 0.08	4.76 ± 0.06	4.82 ± 0.10	3.87 ± 0.08	5.30 ± 0.06
11496569	6.46 ± 0.06	7.73 ± 0.08	6.60 ± 0.01	7.46 ± 0.01	6.41 ± 0.08	5.11 ± 0.09	4.96 ± 0.18	4.28 ± 0.07	5.75 ± 0.06
11550492	6.33 ± 0.06	7.67 ± 0.01	6.53 ± 0.02	7.31 ± 0.02	6.30 ± 0.06	5.02 ± 0.07	4.93 ± 0.12	4.19 ± 0.10	5.65 ± 0.07
11702195	6.01 ± 0.06	7.58 ± 0.03	6.41 ± 0.01	7.18 ± 0.01	6.03 ± 0.05	4.75 ± 0.05	4.78 ± 0.09	3.81 ± 0.10	5.20 ± 0.06
11775511	6.09 ± 0.05	7.54 ± 0.01	6.31 ± 0.13	7.18 ± 0.01	6.14 ± 0.05	4.88 ± 0.06	4.78 ± 0.09	3.99 ± 0.10	5.38 ± 0.06

Table 3 – *continued*

Name	Na/H	Mg/H	Al/H	Si/H	Ca/H	TiI/H	TiII/H	V/H	Cr/H
11819363	6.04 ± 0.14	7.45 ± 0.12	6.22 ± 0.01	7.20 ± 0.01	6.01 ± 0.11	4.69 ± 0.06	4.73 ± 0.12	3.73 ± 0.11	5.25 ± 0.09
12115227	5.69 ± 0.03	7.35 ± 0.02	6.02 ± 0.04	6.99 ± 0.05	5.81 ± 0.04	4.53 ± 0.05	4.55 ± 0.04	3.39 ± 0.06	4.90 ± 0.06
12122151	6.34 ± 0.06	7.66 ± 0.08	6.45 ± 0.01	7.41 ± 0.02	6.28 ± 0.07	4.88 ± 0.06	4.88 ± 0.13	4.00 ± 0.08	5.59 ± 0.08
12647227	5.90 ± 0.05	7.20 ± 0.07	6.06 ± 0.01	7.02 ± 0.02	5.83 ± 0.03	4.49 ± 0.05	4.57 ± 0.08	3.49 ± 0.07	5.09 ± 0.03
1433803	7.64 ± 0.13	7.76 ± 0.22	5.39 ± 0.13	6.55 ± 0.10	2.28 ± 0.04	2.64 ± 0.06	1.87 ± 0.14	1.03 ± 0.08	1.84 ± 0.09
2451509	7.35 ± 0.12	7.21 ± 0.12	4.84 ± 0.11	6.08 ± 0.08	2.00 ± 0.13	2.71 ± 0.01	1.85 ± 0.09	0.91 ± 0.13	1.71 ± 0.13
2970584	7.17 ± 0.12	7.00 ± 0.12	4.89 ± 0.12	6.01 ± 0.10	1.71 ± 0.03	2.48 ± 0.02	1.44 ± 0.04	0.61 ± 0.04	1.32 ± 0.01
3429738	7.09 ± 0.09	6.99 ± 0.11	4.79 ± 0.11	5.90 ± 0.07	1.62 ± 0.02	2.25 ± 0.01	1.36 ± 0.03	0.58 ± 0.02	1.22 ± 0.01
3539408	7.27 ± 0.08	7.14 ± 0.06	4.74 ± 0.11	6.04 ± 0.08	1.93 ± 0.01	2.47 ± 0.02	1.93 ± 0.03	0.88 ± 0.01	1.54 ± 0.01
3644223	7.29 ± 0.12	7.25 ± 0.13	4.83 ± 0.13	6.05 ± 0.08	1.85 ± 0.05	2.36 ± 0.03	1.80 ± 0.09	0.80 ± 0.13	1.50 ± 0.16
3661494	7.12 ± 0.08	6.99 ± 0.06	4.65 ± 0.14	5.92 ± 0.08	1.66 ± 0.03	2.22 ± 0.02	1.59 ± 0.03	0.58 ± 0.03	1.22 ± 0.01
3744043	7.14 ± 0.08	6.99 ± 0.08	4.66 ± 0.12	5.93 ± 0.08	1.70 ± 0.03	–	1.65 ± 0.03	0.67 ± 0.01	1.30 ± 0.01
4055294	7.67 ± 0.12	7.37 ± 0.18	5.31 ± 0.16	6.47 ± 0.12	2.12 ± 0.09	2.96 ± 0.01	1.92 ± 0.11	0.97 ± 0.07	1.75 ± 0.10
4648485	7.42 ± 0.10	7.32 ± 0.10	5.06 ± 0.13	6.23 ± 0.12	1.95 ± 0.06	2.57 ± 0.01	1.80 ± 0.04	0.90 ± 0.01	1.59 ± 0.02
4756219	7.25 ± 0.10	7.21 ± 0.11	4.88 ± 0.16	6.04 ± 0.07	1.79 ± 0.02	2.32 ± 0.01	1.60 ± 0.04	0.71 ± 0.01	1.41 ± 0.01
4826087	7.40 ± 0.12	7.25 ± 0.19	4.99 ± 0.10	6.16 ± 0.08	2.07 ± 0.07	2.73 ± 0.03	1.91 ± 0.10	0.96 ± 0.05	1.76 ± 0.17
4913049	7.43 ± 0.09	7.17 ± 0.11	5.19 ± 0.21	6.23 ± 0.10	2.02 ± 0.01	2.69 ± 0.01	1.97 ± 0.03	0.88 ± 0.02	1.55 ± 0.01
4931389	7.61 ± 0.10	7.33 ± 0.09	5.23 ± 0.14	6.42 ± 0.09	2.14 ± 0.03	2.88 ± 0.01	2.06 ± 0.04	0.98 ± 0.05	1.64 ± 0.04
5265256	7.24 ± 0.10	7.16 ± 0.10	4.81 ± 0.12	5.99 ± 0.08	1.75 ± 0.04	2.34 ± 0.02	1.56 ± 0.03	0.71 ± 0.01	1.45 ± 0.08
5769244	7.58 ± 0.10	7.44 ± 0.16	5.28 ± 0.17	6.43 ± 0.14	2.24 ± 0.01	2.74 ± 0.01	2.09 ± 0.04	0.94 ± 0.04	1.70 ± 0.01
5882005	7.34 ± 0.11	7.27 ± 0.14	4.88 ± 0.10	6.07 ± 0.10	1.97 ± 0.15	2.46 ± 0.01	1.78 ± 0.11	0.86 ± 0.13	1.59 ± 0.10
5940060	7.05 ± 0.10	6.95 ± 0.10	4.76 ± 0.11	5.87 ± 0.10	1.60 ± 0.06	2.30 ± 0.02	1.39 ± 0.04	0.57 ± 0.01	1.20 ± 0.01
6365511	6.88 ± 0.09	6.79 ± 0.08	4.52 ± 0.11	5.72 ± 0.06	1.29 ± 0.04	2.12 ± 0.01	1.17 ± 0.03	0.41 ± 0.03	0.96 ± 0.01
6547007	6.68 ± 0.08	6.66 ± 0.08	4.29 ± 0.08	5.47 ± 0.06	1.16 ± 0.02	–	1.05 ± 0.03	0.29 ± 0.03	0.85 ± 0.03
6851499	7.11 ± 0.10	7.05 ± 0.09	4.71 ± 0.10	5.91 ± 0.11	1.66 ± 0.04	2.27 ± 0.01	1.49 ± 0.03	0.60 ± 0.02	1.29 ± 0.02
6859803	7.33 ± 0.12	7.22 ± 0.13	4.83 ± 0.11	6.09 ± 0.14	2.13 ± 0.17	2.59 ± 0.01	1.87 ± 0.08	0.97 ± 0.01	1.60 ± 0.14
6964342	7.41 ± 0.13	7.36 ± 0.22	5.08 ± 0.13	6.25 ± 0.14	2.06 ± 0.18	2.63 ± 0.01	1.69 ± 0.12	0.88 ± 0.07	1.66 ± 0.09
7429055	7.41 ± 0.10	7.33 ± 0.13	5.13 ± 0.18	6.26 ± 0.10	2.08 ± 0.01	2.53 ± 0.02	1.80 ± 0.03	0.83 ± 0.02	1.60 ± 0.08
7430868	7.16 ± 0.11	7.12 ± 0.11	4.88 ± 0.14	6.00 ± 0.10	1.77 ± 0.03	2.26 ± 0.01	1.53 ± 0.03	0.63 ± 0.02	1.29 ± 0.02
7450230	7.37 ± 0.08	7.17 ± 0.08	5.00 ± 0.16	6.16 ± 0.08	1.93 ± 0.02	2.51 ± 0.01	1.84 ± 0.03	0.77 ± 0.05	1.48 ± 0.01
7533995	7.42 ± 0.11	7.36 ± 0.11	5.09 ± 0.17	6.26 ± 0.11	2.06 ± 0.05	2.51 ± 0.04	1.86 ± 0.03	0.86 ± 0.03	1.58 ± 0.01
7617227	7.17 ± 0.08	7.07 ± 0.06	4.69 ± 0.13	5.97 ± 0.07	1.74 ± 0.04	2.28 ± 0.01	1.66 ± 0.04	0.59 ± 0.05	1.30 ± 0.01
7812552	6.98 ± 0.08	6.80 ± 0.07	4.57 ± 0.09	5.79 ± 0.07	1.53 ± 0.02	–	1.37 ± 0.01	–	–
8129047	7.42 ± 0.11	7.18 ± 0.11	5.12 ± 0.20	6.27 ± 0.11	2.16 ± 0.01	2.67 ± 0.02	1.92 ± 0.03	0.85 ± 0.01	1.59 ± 0.05
8493969	7.16 ± 0.09	7.00 ± 0.08	4.84 ± 0.16	5.99 ± 0.09	1.73 ± 0.02	2.33 ± 0.01	1.59 ± 0.03	0.69 ± 0.03	1.23 ± 0.03
8587329	7.64 ± 0.12	7.86 ± 0.21	5.39 ± 0.17	6.54 ± 0.11	2.38 ± 0.13	2.45 ± 0.03	2.07 ± 0.05	0.96 ± 0.07	1.82 ± 0.05
8590920	7.68 ± 0.11	7.83 ± 0.26	5.47 ± 0.16	6.59 ± 0.11	2.42 ± 0.11	2.71 ± 0.01	1.98 ± 0.07	0.87 ± 0.05	1.82 ± 0.11
8612241	7.27 ± 0.12	7.09 ± 0.13	4.87 ± 0.11	6.03 ± 0.09	1.79 ± 0.15	2.40 ± 0.01	1.57 ± 0.07	0.83 ± 0.11	1.44 ± 0.07
8737032	7.29 ± 0.11	7.23 ± 0.16	4.87 ± 0.12	6.05 ± 0.10	1.89 ± 0.07	2.50 ± 0.02	1.68 ± 0.10	0.88 ± 0.07	1.58 ± 0.14
9080175	6.95 ± 0.08	6.85 ± 0.09	4.71 ± 0.14	5.78 ± 0.08	1.45 ± 0.04	2.17 ± 0.01	1.22 ± 0.03	0.36 ± 0.06	1.04 ± 0.04
9145955	7.20 ± 0.11	7.09 ± 0.10	4.74 ± 0.13	5.96 ± 0.06	1.72 ± 0.03	–	1.75 ± 0.12	0.77 ± 0.10	1.48 ± 0.04
9535399	7.62 ± 0.15	7.55 ± 0.20	5.37 ± 0.23	6.54 ± 0.12	2.37 ± 0.16	2.75 ± 0.01	2.11 ± 0.04	0.92 ± 0.07	1.73 ± 0.06
9640480	7.10 ± 0.08	6.87 ± 0.09	4.85 ± 0.18	5.90 ± 0.08	1.69 ± 0.02	2.35 ± 0.01	1.49 ± 0.03	0.58 ± 0.04	1.17 ± 0.02
9711269	7.57 ± 0.10	7.37 ± 0.13	5.22 ± 0.21	6.40 ± 0.11	2.28 ± 0.03	2.79 ± 0.01	2.07 ± 0.03	0.94 ± 0.01	1.69 ± 0.05
9772366	7.64 ± 0.11	7.49 ± 0.15	5.37 ± 0.21	6.54 ± 0.10	2.36 ± 0.02	2.80 ± 0.01	2.09 ± 0.05	0.91 ± 0.06	1.67 ± 0.15
9777293	6.89 ± 0.09	6.77 ± 0.09	4.54 ± 0.09	5.70 ± 0.06	1.43 ± 0.02	–	1.19 ± 0.03	–	0.96 ± 0.01
9783226	7.48 ± 0.13	7.32 ± 0.19	5.05 ± 0.14	6.30 ± 0.11	2.17 ± 0.08	2.64 ± 0.01	1.97 ± 0.11	0.86 ± 0.08	1.68 ± 0.06
9967700	7.08 ± 0.08	6.96 ± 0.07	4.63 ± 0.09	5.87 ± 0.10	1.63 ± 0.01	–	1.62 ± 0.03	0.53 ± 0.01	1.21 ± 0.01
10095427	6.95 ± 0.09	6.87 ± 0.10	4.69 ± 0.15	5.79 ± 0.07	1.54 ± 0.04	2.20 ± 0.02	1.23 ± 0.04	0.33 ± 0.06	0.95 ± 0.01
10351820	7.38 ± 0.12	7.29 ± 0.16	4.92 ± 0.10	6.14 ± 0.10	2.05 ± 0.08	2.59 ± 0.02	1.83 ± 0.09	0.91 ± 0.15	1.66 ± 0.03
10513837	7.54 ± 0.12	7.41 ± 0.16	5.09 ± 0.10	6.32 ± 0.10	2.14 ± 0.01	2.83 ± 0.03	1.88 ± 0.11	0.93 ± 0.12	1.71 ± 0.02
10550429	7.52 ± 0.09	7.29 ± 0.10	5.07 ± 0.15	6.30 ± 0.10	2.18 ± 0.10	2.80 ± 0.02	2.03 ± 0.05	0.92 ± 0.05	1.60 ± 0.01
10659842	7.28 ± 0.11	7.12 ± 0.14	4.81 ± 0.13	6.01 ± 0.10	1.90 ± 0.04	2.53 ± 0.02	1.87 ± 0.09	0.86 ± 0.09	1.53 ± 0.19
10722175	7.61 ± 0.13	7.59 ± 0.20	5.30 ± 0.14	6.50 ± 0.11	2.32 ± 0.08	2.78 ± 0.02	1.82 ± 0.16	0.95 ± 0.15	1.74 ± 0.02
10793771	7.55 ± 0.11	7.39 ± 0.18	5.10 ± 0.12	6.30 ± 0.10	2.19 ± 0.10	2.85 ± 0.01	2.02 ± 0.11	1.03 ± 0.08	1.74 ± 0.08
10801063	7.15 ± 0.09	6.97 ± 0.08	4.81 ± 0.13	5.97 ± 0.10	1.76 ± 0.04	2.33 ± 0.02	1.61 ± 0.03	–	1.19 ± 0.01
10992711	7.06 ± 0.10	6.95 ± 0.13	4.79 ± 0.13	5.88 ± 0.08	1.61 ± 0.01	2.25 ± 0.01	1.35 ± 0.03	0.50 ± 0.02	1.19 ± 0.02
11020211	7.10 ± 0.08	6.94 ± 0.09	4.71 ± 0.14	5.91 ± 0.08	1.68 ± 0.05	2.29 ± 0.06	1.53 ± 0.03	0.51 ± 0.01	1.13 ± 0.01
11029423	7.34 ± 0.10	7.27 ± 0.12	5.05 ± 0.15	6.14 ± 0.08	1.92 ± 0.03	2.45 ± 0.01	1.74 ± 0.04	0.78 ± 0.02	1.53 ± 0.01
11087371	7.64 ± 0.10	7.55 ± 0.13	5.43 ± 0.19	6.54 ± 0.10	2.30 ± 0.02	–	2.00 ± 0.04	0.81 ± 0.03	1.69 ± 0.01
11228549	6.67 ± 0.09	6.59 ± 0.07	4.29 ± 0.09	5.50 ± 0.06	1.14 ± 0.02	–	0.93 ± 0.03	0.43 ± 0.01	0.92 ± 0.28
11250139	6.97 ± 0.09	6.89 ± 0.09	4.61 ± 0.11	5.80 ± 0.08	1.53 ± 0.06	2.17 ± 0.01	1.31 ± 0.03	0.45 ± 0.05	1.14 ± 0.03
11358669	7.61 ± 0.13	7.39 ± 0.19	5.29 ± 0.13	6.46 ± 0.12	2.16 ± 0.09	2.95 ± 0.02	1.95 ± 0.12	1.02 ± 0.08	1.76 ± 0.03
11453721	7.08 ± 0.12	7.06 ± 0.10	4.77 ± 0.13	5.91 ± 0.06	1.63 ± 0.05	2.18 ± 0.01	1.41 ± 0.04	0.49 ± 0.02	1.21 ± 0.01

Table 3 – *continued*

Name	Na/H	Mg/H	Al/H	Si/H	Ca/H	TiI/H	TiII/H	V/H	Cr/H
11496569	7.47 ± 0.14	7.26 ± 0.17	5.08 ± 0.12	6.22 ± 0.11	2.19 ± 0.03	2.88 ± 0.04	1.92 ± 0.12	0.90 ± 0.09	1.75 ± 0.23
11550492	7.43 ± 0.10	7.24 ± 0.10	5.01 ± 0.16	6.24 ± 0.11	2.03 ± 0.06	2.59 ± 0.01	1.92 ± 0.04	0.82 ± 0.01	1.53 ± 0.01
11702195	6.99 ± 0.10	6.92 ± 0.11	4.76 ± 0.16	5.82 ± 0.08	1.57 ± 0.05	2.18 ± 0.01	1.29 ± 0.03	0.50 ± 0.06	1.08 ± 0.03
11775511	7.18 ± 0.09	6.98 ± 0.10	4.81 ± 0.17	5.96 ± 0.09	1.73 ± 0.06	2.37 ± 0.03	1.64 ± 0.03	0.63 ± 0.08	1.29 ± 0.01
11819363	7.13 ± 0.12	7.00 ± 0.12	4.68 ± 0.13	5.89 ± 0.10	1.70 ± 0.14	2.30 ± 0.01	1.69 ± 0.08	0.63 ± 0.14	1.29 ± 0.08
12115227	6.73 ± 0.09	6.66 ± 0.08	4.32 ± 0.08	5.54 ± 0.06	1.39 ± 0.03	–	1.14 ± 0.03	–	0.88 ± 0.01
12122151	7.35 ± 0.13	7.29 ± 0.17	4.97 ± 0.12	6.12 ± 0.10	2.05 ± 0.12	2.55 ± 0.04	1.81 ± 0.10	0.90 ± 0.06	1.60 ± 0.04
12647227	6.96 ± 0.08	6.89 ± 0.08	4.48 ± 0.11	5.76 ± 0.06	1.53 ± 0.02	2.02 ± 0.01	1.49 ± 0.01	0.43 ± 0.01	1.12 ± 0.01

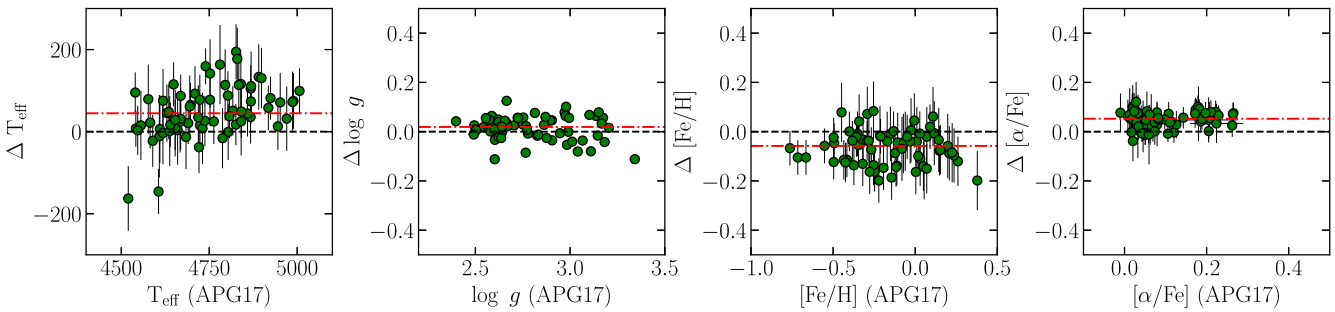

Figure 1. Comparison between the atmospheric parameters and [α/Fe] of APOGEE (APG17) and those found in this work for the sample of *Kepler* stars. The difference Δ on *y*-axis is (this work) – APG17. The dash–dotted line is the average offset.

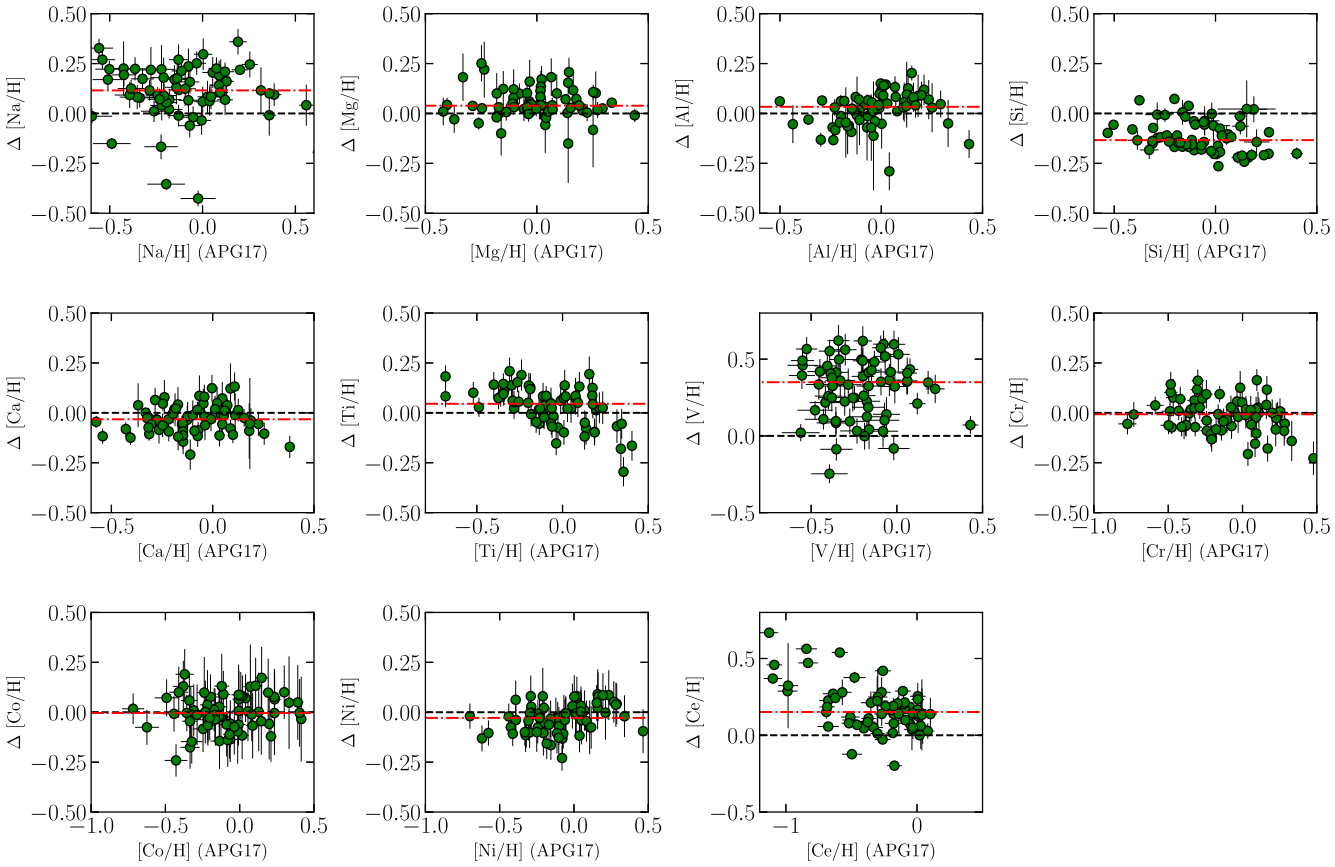

Figure 2. Comparison between the elemental abundances of APOGEE (APG17) and those found in this work for the sample of *Kepler* stars. The difference Δ on *y*-axis is (this work) – APG17. The dash–dotted line is the average offset.

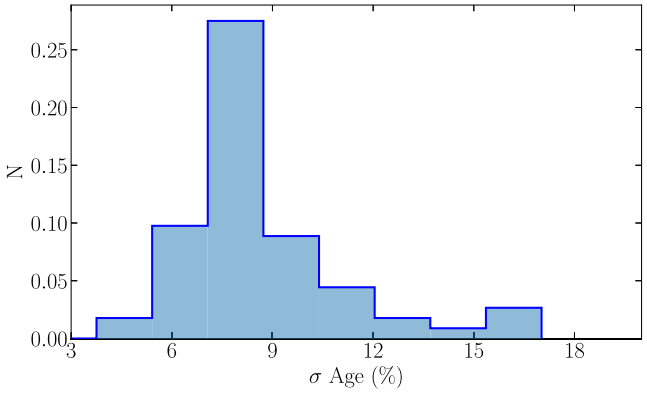

Figure 3. Uncertainties distribution for the age computed using the individual mode frequencies for our *Kepler* sample. *N* is a probability density: each bin displays the number of stars per bin divided by the total number of stars and the bin width.

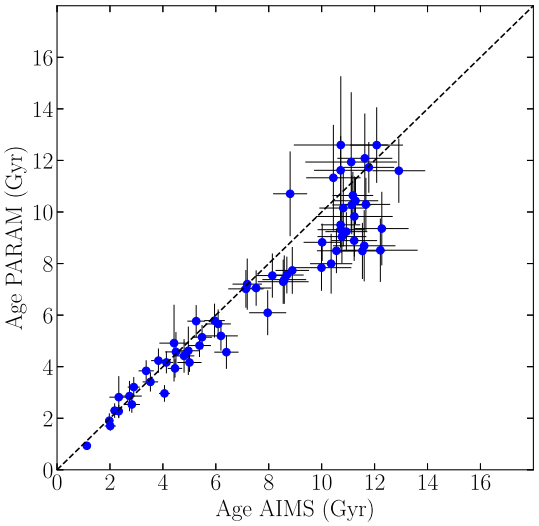

Figure 4. Comparison between asteroseismic ages of our sample of *Kepler* stars computed using individual mode frequencies (AIMS) and using $\nu_{\max}$ and $\Delta\nu$ by PARAM.

to 1.7 Gyr in the oldest age regime (> 10 Gyr), showing a younger thick disc compared to its estimated average age of around 11 Gyr (Mackereth et al. 2021; Miglio et al. 2021; Queiroz et al. 2023; Gallart et al. 2024). This might be due to a systematic overestimation of mass in APOKASC3 with respect to individual mode frequencies, that yield mass consistent with well-studied eclipsing binaries present in literature (Brogaard et al. 2018, 2022; Jørgensen et al. 2021; Thomsen et al. 2025).

2.4 Spatial distribution

Our stars are located in the solar neighbourhood ($7.5 < R_{GC} < 8.5$ kpc). None the less, they could have come from other regions of the Galactic disc, transiting into the solar vicinity, or could have migrated in previous epochs due to the change in their eccentricity through radial heating or in their angular momentum (Lynden-Bell & Kalnajs 1972; Sellwood & Binney 2002). To better understand their provenance, we computed the guiding radius R_g, which is the radius of a circular orbit with specific angular momentum L_z (estimated as $R_g = R_{GC} \cdot V/V_{LSR}$, where V is the Galactocentric azimuthal velocity and V_{LSR} is the circular velocity at the solar Galactocentric distance). Moreover, the adoption of R_g instead of the Galactocentric radius R_{GC} can mitigate the blurring effect due to epicyclic oscillations around the guiding radius (Schönrich & Binney 2009). However, it cannot overcome the migrating effect due to churning, which can change R_g due to interactions with spiral arms or bars (Sellwood & Binney 2002; Binney & Tremaine 2008). The guiding radius is computed from the stellar orbits obtained using the GALPY package of PYTHON, in which the model MWPOTENTIAL2014 for the gravitational potential of the Milky Way is assumed (Bovy 2015). Through the astrometric information by *Gaia* DR3, distances from Bailer-Jones et al. (2021),[4] an assumed solar Galactocentric distance $R_0 = 8$ kpc, a height above the plane $z_0 = 0.025$ kpc (Jurić et al. 2008), a circular velocity at the solar Galactocentric distance equal to $V_{LSR} = 220$ kms^{-1}, and the Sun's motion with respect to the local standard of rest $[U_\odot, V_\odot, W_\odot] = [11.1, 12.24, 7.25]$ kms^{-1} (Schönrich, Binney & Dehnen 2010), we obtained the orbital parameters, among which the guiding radius R_g. The distribution of R_g of the data set is shown in Fig. 5. It is peaked at 8 kpc with an extension to 4 kpc in the inner disc and more than 9 kpc in the outer disc.

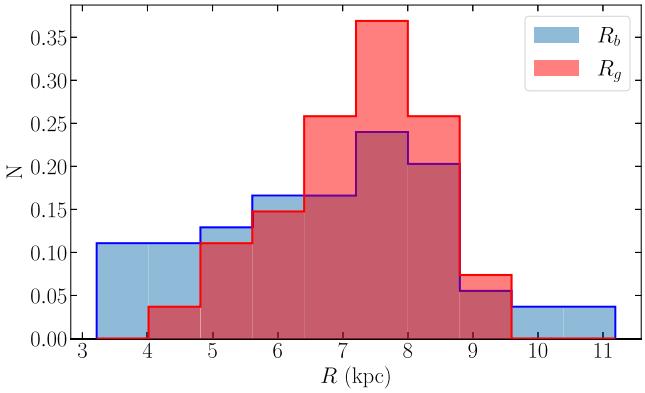

Figure 5. Distribution of R_g and R_b for the *Kepler* sample. *N* is a probability density as in Fig. 3.

2.4.1 *Birth radii*

To better constrain radial migration, recent works in literature (Ratcliffe et al. 2023; Lu et al. 2024) estimated the birth radii (distances between the birth location of a star and the centre of the Milky Way) using stellar ages and metallicities. Knowing the birth radius can provide us with details on the evolution of the abundance gradient over time and, consequently, on the assembly history of our Galaxy, as well as the origin of the high- and low-α sequences.

The empirical method explained in Lu et al. (2024) assumes a linear relation between the present-day metallicity range and the birth radial metallicity gradient, inferred from cosmological simulations of disc formation. According to this approach, for any lookback time τ, the metallicity can be written as a function of the metallicity gradient at that time ∇[Fe/H] (τ), birth radius and the metallicity at the Galactic centre [Fe/H] (0, τ). To estimate [Fe/H] (0, τ), Lu et al. (2024) used the upper boundary of the age–metallicity relation for stars currently found in the inner Milky Way disc. While the use of birth radii can

[4]We also tested asteroseismic distances from param: the use of param distances in the calculation results in an average difference in guiding radius R_g of 0.002 kpc with standard deviation of 0.013 kpc.

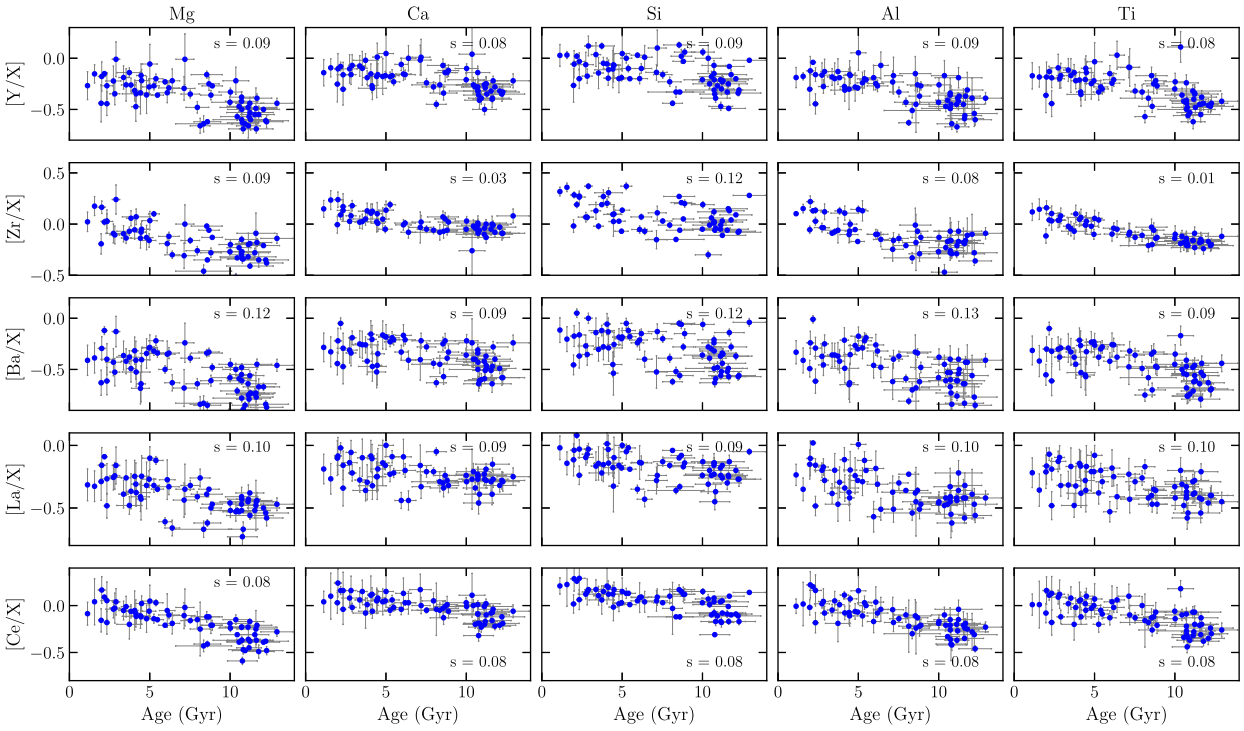

Figure 6. Chemical clocks [s/α] versus stellar age for the *Kepler* sample. Different rows have different *s*-process elements, while different columns have different α-elements. The scatter is indicated in each panel.

provide interesting insights, as by definition they are unaffected by radial migration, it should be kept in mind that their use strongly relies on the aforementioned assumptions used to derive them.

Fig. 5 displays the radii distribution for R_g and R_b. R_b is computed using the equation (3) in Lu et al. (2024), where we used metallicity and stellar age from our sample, while [Fe/H] $(0, \tau)$ from their table 1.

The R_g distribution is peaked at 8 kpc, while the R_b distribution is more flat and widens at smaller and larger radii than R_g one. In the next sections, we will study the chemical clocks relations using different bins in R_g and R_b.

3 CHEMICAL CLOCKS

The ratios of *s*-process elements to α-elements are widely studied as age indicators because they show a steeper trend with age compared to [s/Fe] and [α/Fe]. In Fig. 6, we show the trends of all chemical clocks that we can compose using the *s*- and α-elements that we have at our disposal. They are respectively: Y, Zr, Ba, La, and Ce[5]; Mg, Ca, Si, Ti, and the odd-Z Al (it has a similar behaviour to α-elements). All of the abundance ratios display a decreasing trend with increasing stellar age. This is expected due to the *s*-over-α-elements ratio and their different nucleosynthetic origins.

Among the different abundance ratios, those composed by Zr and Ce show the smaller scatter with ages. Particularly, the tightest relation of Zr is with Ti with an intrinsic scatter of 0.01 dex. The trends including Ce have the same intrinsic scatter of ∼0.08 dex, consistent across all α-elements. La and Ba are the element that reveal the largest scatter (∼ 0.1 dex) among the *s*-elements, whereas Y has a intrinsic scatter of ∼ 0.085 dex. The large scatter observed for Ba is likely due to the measurement of a single spectral line, 5853.668 Å, which may be saturated.

From this point onward, we focus on [Ce/Mg][6] and [Zr/Ti] only, as they exhibit the least scatter among chemical clocks and since Zr and Ce are, respectively, two *s*-process elements of the first and second peak in the periodic table. We selected one *s*-process element for each peak, as they exhibit different dependencies on metallicity and stellar age; consequently, the associated chemical clocks might also differ. In addition, Ce is the only *s*-process element available in the APOGEE survey, which is another reason to include it in this work.

Using the R_g and R_b estimations in Section 2.4, we examined the trends of [Zr/Ti] and [Ce/Mg] at different radii. In Fig. 7, we present [Zr/Ti] and [Ce/Mg] versus radii, where the mono-age populations are highlighted using running means, which were obtained by averaging [Ce/Mg] and [Zr/Ti] for different radius and age bins. The figure shows that the youngest mono-age populations have higher abundance ratios, while the oldest mono-age populations have lower content in each panel. In addition, the oldest mono-age population is more spread out in R_g due to the radial migration. Since older stars have had more time to experience these effects, they are more likely to have drifted significantly from their original location. This results in a wider radial distribution for old stars compared to younger ones. Moreover, the running means do not show different slopes at different age for [Zr/Ti]. Mono-age populations show flat abundance ratios as function of R_g and R_b, suggesting that spatial correlations are secondary, thus reinforcing the suitability of these ratios as chemical clocks. The situation is slightly different

[5]We did not use Sr since it was measured for a few stars. Pr and Nd are considered *s*-process elements but their *r*-component is higher than the other *s*-process studied in this work.

[6]Despite Ce having a small scatter with all α-elements in this study, we focus on [Ce/Mg] as Mg is the α-element with the most measurements available in the APOGEE survey.

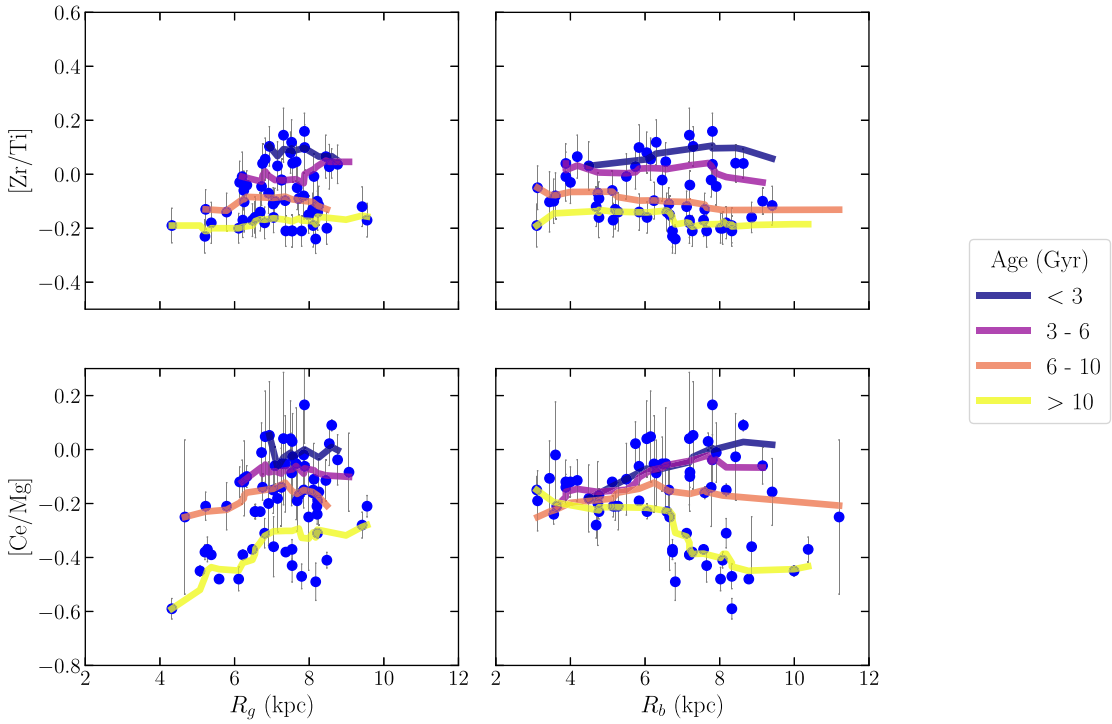

Figure 7. Radial gradients of [Zr/Ti] (top panels) and [Ce/Mg] (bottom panels) for the *Kepler* sample. The lines are the running means of different mono-age populations, determined by calculating the average of [Zr/Ti] and [Ce/Mg] for different bins of R_g (left panels) and R_b (right panels).

for [Ce/Mg] panels where the mono-age populations have a positive radial gradient, except for the oldest mono-aged populations in the R_b panel, corresponding to the high-αsequence. A similar behaviour is observed in Ratcliffe et al. (2023) for [Ce/Mg] – lesser extent for Y, an *s*-process element of the first peak like Zr – where they interpret this radial gradient as an evidence of a rapid increase in the enrichment with Galactic radius. Moreover, the different behaviour of Ce with respect to Zr is due to the different yields dependence on metallicity (and as a consequence on radius because of the radial metallicity gradient).

Fig. 8 shows the age–[Zr/Ti] and [Ce/Mg] relations for stars born at different locations in the Galaxy. Following Casali et al. (2023) and Ratcliffe et al. (2023) that studied chemical clocks composed by Ce, Ba, and Y, we would expect a flattening for the most internal mono-R_b populations (less prominent for the mono-R_g populations) and an increase in the slopes for the mono-R_b populations at larger radii. This effect is more evident for the *s*-process of the second peak, such as Ce and Ba, while is less evident for element of the second peak, such as Y and Zr. In our work, we found a similar behaviour: the abundance ratios are almost flat in the inner regions and steeper moving towards the outer regions for the R_b bins (we do not have the innermost R_g bin); this behaviour is more evident for [Ce/Mg] with respect to [Zr/Ti]. Indeed, Zr is an *s*-process of the first peak for which the flattening of the innermost mono-R_b population is less pronounced. Furthermore, Zr has a relevant r-component, which could make all slopes similar.

3.1 [s/α]–[Fe/H]–age relations

In this section, we investigate [s/α]–[Fe/H]–age trends for the stars in our sample, dividing stars in R_g and R_b. The aim of this section is to use these relations to derive ages for a large sample of stars in spectroscopic surveys. We focused on [Zr/Ti] and [Ce/Mg] only, since they are the ratios with the smallest scatter.

We modelled the [s/α] distributions at different R_g (or R_b) bins, also taking into account the [Fe/H] dependence as follows:

$$[s/\alpha] = m_1 \cdot \mathrm{Age} + m_2 \cdot [\mathrm{Fe/H}] + c \quad (2)$$

where m_1, m_2, and c are in Table 4. The bins are, respectively, $R_g < 7$ kpc, $7 \leq R_g \leq 8$ kpc, $R_g > 8$ kpc, and $R_b < 6$ kpc, $6 \leq R_b \leq 7$ kpc, and $R_b > 7$ kpc. The different separation between the two radii is related to the different distribution for R_g and R_b. The bins were chosen by considering the three regions of the disc – inner, solar, outer – and by returning a similar number of stars per bin.

In our calculation, we took into account the uncertainties on [s/α], [Fe/H], and stellar age. The best fits with the spread (68 per cent confidence interval plus intrinsic scatter) of the models resulting from the posteriors are represented in Fig. 9 for [Zr/Ti] and Fig. 10 for [Ce/Mg] with a black line and a red shaded area, respectively, for the bins in R_g and R_b (relations at [Fe/H] = 0 are shown). The values of all relations are shown in Table 4. The [Fe/H] colour-coding of these stars show a dependence on metallicity. We can see that stars with lower metallicity have higher [s/α] at a given age. This behaviour was already shown in Feltzing et al. (2017), Delgado Mena et al. (2019), Casali et al. (2020, 2023), and Magrini et al. (2021), suggesting that the metallicity dependence is due to the different star formation history and the non-monotonic dependence of *s*-process yields on [Fe/H] (Busso et al. 2001; Cristallo et al. 2015; Vescovi et al. 2020).

Fig. 9 shows the chemical clock [Zr/Ti] versus stellar age divided in bins of R_g (left panels) and R_b (right panels). Regarding the R_g bins, the slopes with ages are consistent within the errors (see m_1 in Table 4). This could be attributed to the R_g distribution, which has fewer stars at the smallest and largest radii ($R_g < 6$ and $R_g > 8.5$ kpc). Most stars are concentrated near to the solar region (around

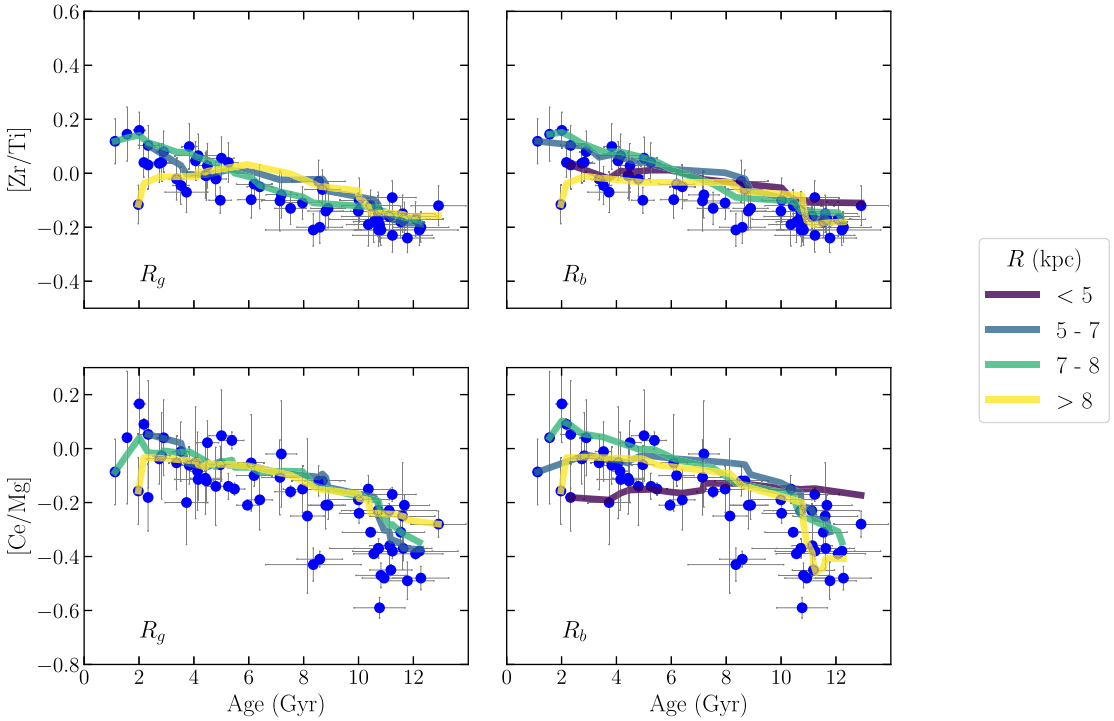

Figure 8. [Zr/Ti] (top panels) and [Ce/Mg] (bottom panels) versus stellar age. The lines are the running means of mono-R_g populations (left panels) and mono-R_b populations (right panels).

Table 4. Parameters of the MCMC fitting.

Ratio	Bin	m_1 (dex/Gyr)	m_2 (dex)	c (dex)	ϵ (dex)
[Zr/Ti]	$R_g < 7$ kpc	-0.020 ± 0.006	0.072 ± 0.094	0.085 ± 0.048	0.014 ± 0.013
[Zr/Ti]	$7 \leq R_g \leq 8$ kpc	-0.022 ± 0.005	0.150 ± 0.078	0.115 ± 0.033	0.016 ± 0.014
[Zr/Ti]	$R_g > 8$ kpc	-0.023 ± 0.005	0.173 ± 0.112	0.119 ± 0.048	0.019 ± 0.017
[Zr/Ti]	$R_b < 6$ kpc	-0.023 ± 0.007	-0.066 ± 0.188	0.112 ± 0.057	0.017 ± 0.015
[Zr/Ti]	$6 \leq R_b \leq 7$ kpc	-0.021 ± 0.013	0.283 ± 0.377	0.130 ± 0.050	0.019 ± 0.018
[Zr/Ti]	$R_b > 7$ kpc	-0.016 ± 0.005	0.287 ± 0.138	0.127 ± 0.037	0.013 ± 0.012
[Zr/Ti]	No binning	-0.022 ± 0.003	0.123 ± 0.048	0.104 ± 0.022	0.009 ± 0.008
[Ce/Mg]	$R_g < 7$ kpc	-0.028 ± 0.010	0.264 ± 0.093	0.068 ± 0.084	0.073 ± 0.018
[Ce/Mg]	$7 \leq R_g \leq 8$ kpc	-0.036 ± 0.009	0.080 ± 0.136	0.095 ± 0.063	0.080 ± 0.025
[Ce/Mg]	$R_g > 8$ kpc	-0.030 ± 0.008	0.174 ± 0.146	0.068 ± 0.069	0.087 ± 0.025
[Ce/Mg]	$R_b < 6$ kpc	-0.018 ± 0.006	-0.234 ± 0.159	-0.026 ± 0.053	0.034 ± 0.014
[Ce/Mg]	$6 \leq R_b \leq 7$ kpc	-0.030 ± 0.020	0.202 ± 0.497	0.099 ± 0.087	0.062 ± 0.030
[Ce/Mg]	$R_b > 7$ kpc	-0.049 ± 0.008	0.110 ± 0.161	0.188 ± 0.054	0.069 ± 0.019
[Ce/Mg]	No binning	-0.032 ± 0.005	0.194 ± 0.059	0.092 ± 0.037	0.078 ± 0.011

6–8 kpc), suggesting that the stars in the inner and outer bins have radii that are not significantly different from those in the central bin. Moreover, as we discussed in Section 3, Zr is an element of the first peak as Y, which does not show differences at different R_g (see also fig. 2 of Ratcliffe et al. 2023).

When comparing the sample in terms of birth radii and guiding radii, it is observed that more metal-rich stars tend to have smaller birth radii than guiding radii: metal-rich stars are more concentrated in the inner disc, whereas the metal-poor stars in the outer disc. Although the R_b distribution is broader than the R_g distribution, extending to both very small and very large radii, the slopes in the three R_b bins remain still consistent with each other within the errors. They are also consistent with those obtained for the R_g bins. In conclusion, the relations in the three bins in R_g and R_b do not show variation in their slopes, implying no differences in [Zr/Ti]–age relations among inner, solar, and outer regions. For this reason, we also computed the relation taking all the stars together, without dividing them in three spatial bins. The parameters (named 'no binning') are listed in Table 4. This relation shows similar parameters to those for the binned relations within the errors; however, the uncertainties on the parameters and the intrinsic scatter are smaller. Indeed, by increasing number of samples we get a better measurement of the sample variance following the central limit theorem.

Fig. 10 shows the relations for the chemical clock [Ce/Mg]. The slopes in the three R_g regions are consistent within errors as we saw for [Zr/Ti] (the central bin shows a more negative slope), due to the narrow R_g distribution: stars are more concentrated around the solar regions, with their radii not differing significantly from those in the solar bin when compared to the outer and inner bins. However, when

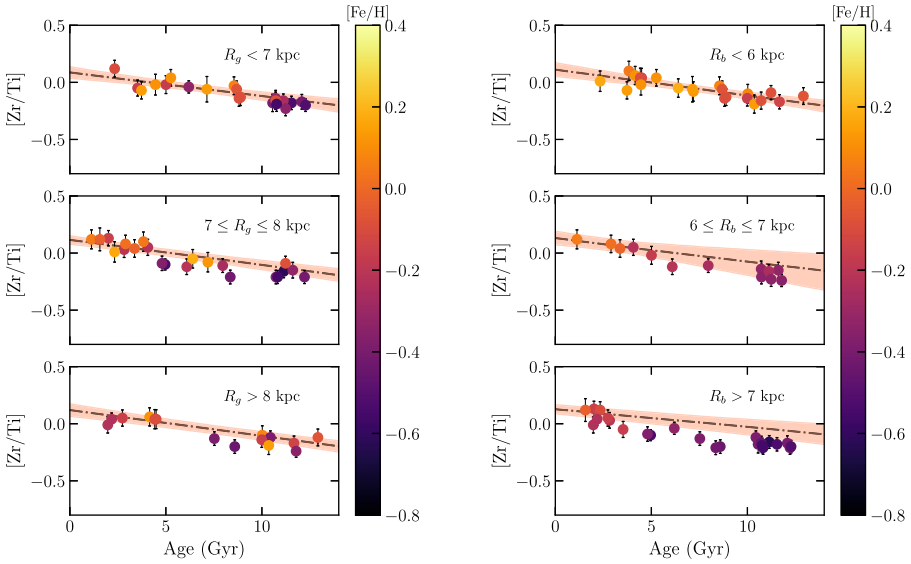

Figure 9. [Zr/Ti] versus stellar age for the *Kepler* sample in different bins of R_g (left panels) and R_b (right panels). The data are colour-coded by metallicity. The dash–dotted line represents the best fit, and the shaded area, the 68 per cent confidence interval plus intrinsic scatter. Although our sample of stars spans a range of metallicities, the fits in the plots are shown for [Fe/H] $= 0$, which may not accurately represent the metallicity of some stars that appear discrepant from the fit.

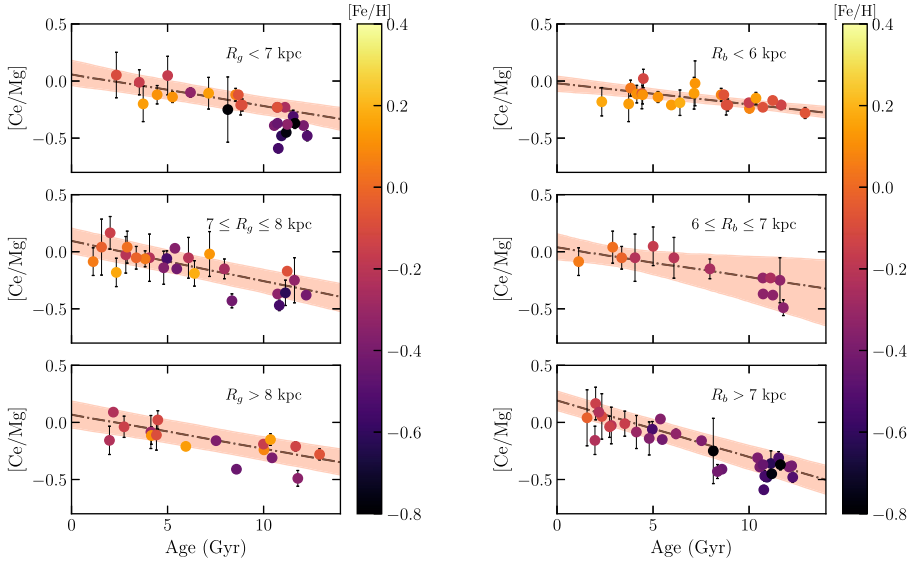

Figure 10. [Ce/Mg] versus stellar age for the *Kepler* sample in different bins of R_g (left panels) and R_b (right panels). The data are colour-coded by metallicity. The dash–dotted line represents the best fit, and the shaded area, the 68 per cent confidence interval plus intrinsic scatter. Although our sample of stars spans a range of metallicities, the fits in the plots are shown for [Fe/H] $= 0$, which may not accurately represent the metallicity of some stars that appear discrepant from the fit.

we look at the distribution in R_b, the situation is different. The inner region is quite flat, whereas the slopes of the relations become steeper moving towards the outer region. This behaviour is already seen in Casali et al. (2023) and Ratcliffe et al. (2023) for Ce, implying a larger dependency on the radial birth position. The intrinsic scatter for the relations binned in R_b is smaller than the intrinsic scatter for the relations binned in R_g, unlike [Zr/Ti].

It is important to note that the high precision ages and abundances derived in this work significantly reduce the scatter found in Casali et al. (2023) when trying to calibrate [Ce/Mg] using APOGEE data with ages from global seismic parameters. This is a sobering example of the power of chemical clocks when high precision data are available. Leveraging on the improved precision of the [Ce/Mg] calibration derived here, we thus apply these relations to the APOGEE sample where the large number of stars available allow a meaningful focus on average age trends (see Section 4).

We estimated the accuracy and precision of each relation in recovering the input age of our sample of stars. We defined the accuracy as the mean average of the relative errors, $(\mathrm{Age_{input}} - \mathrm{Age_{output}})/\mathrm{Age_{input}}$, between input and output ages obtained from our relations, while the precision is its standard deviation (see also Section 3.2). The relations between [Zr/Ti]/[Ce/Mg]–[Fe/H]–age are

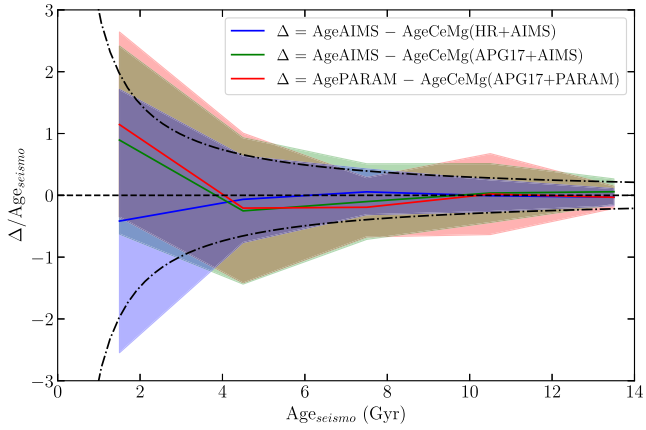

Figure 11. The mean (solid line) and standard deviation (shaded area) of $\Delta/\mathrm{Age}_{\mathrm{seismo}}$ in different age bins, where Δ is explained in the legend. $\mathrm{Age}_{\mathrm{seismo}}$ is AgeAIMS or AgePARAM depending on the left term of the Δ. The dot–dashed lines indicate the relative error in ages for an absolute uncertainty of 2.95 Gyr.

able to reproduce the asteroseismic ages of our sample with an overall accuracy and precision of 7 per cent and 60 per cent for [Zr/Ti], and 7 per cent and 70 per cent for [Ce/Mg]. However, it is worth pointing out that accuracy and precision change considerably as a function of age (since the denominator of the relative error is small for young ages and large for old ages), whereby above 5 Gyr typical accuracy and precision for chemical clocks is of the order of 0.3 per cent and 25 per cent for [Zr/Ti] and 3 per cent and 35 per cent for [Ce/Mg], respectively. Typical input uncertainties to build these relations are 0.06 dex in [Zr/Ti], 0.08 dex in [Ce/Mg], 0.04 in [Fe/H], and 8 per cent in stellar age.

In summary, it is important to emphasize that chemical ages are inherently statistical. They can be used to estimate age distributions or trends across stellar populations, but their usability for individual stars is limited by the precision. Further tests on the accuracy and precision of chemical ages using data of different quality are discussed in the next section.

3.2 High precision for calibrators

To highlight the significance of the high-precision abundances and ages used in this work to calibrate chemical clocks, we examined how the tightest of these relations would degrade when using input data of lower quality. Using the same technique discussed in Section 3.1, here we derived the [Ce/Mg]–[Fe/H]–age relations for the sample of 68 *Kepler* stars, using ages from individual mode frequencies, but Ce and Mg abundances from APOGEE DR17 instead.[7] These relations have an average intrinsic scatter of ~ 0.15 dex, against the ~ 0.08 dex when using our abundances instead.

Finally, for the same 68 *Kepler* stars we performed a recovery test comparing chemical ages inferred from [Ce/Mg] against input asteroseismic ages used to build the relations. These results are shown in Fig. 11, where the mean and standard deviation of the recovered ages are shown for the following cases:

[7]Albeit the relation with [Zr/Ti] is even tighter than the one using [Ce/Mg], we focus on the latter since the only survey overlapping with our sample is APOGEE for which Zr is not available.

(i) high-precision abundances from this work with high-precision ages from individual mode frequencies (blue line and shade. Hereafter: chemical ages HR + AIMS);

(ii) abundances from APOGEE DR17 with high-precision ages from individual mode frequencies (green line and shade. Hereafter: chemical ages APG17 + AIMS);

(iii) abundances from APOGEE DR17 with ages from global asteroseismic parameters, ν_{max} and $\Delta\nu$ (red line and shade. Hereafter: chemical ages APG17 + PARAM).

To estimate the accuracy and precision of the chemical ages, we calculated the mean and standard deviation of the relative errors of the chemical ages compared to the seismic ages:

$$\frac{\mathrm{Age}_{\mathrm{seismo}} - \mathrm{Age}_{\mathrm{chemical}}}{\mathrm{Age}_{\mathrm{seismo}}}, \tag{3}$$

where $\mathrm{Age}_{\mathrm{chemical}}$ are chemical ages (from HR+AIMS, APG17+AIMS, or APG17 + PARAM), and $\mathrm{Age}_{\mathrm{seismo}}$ are ages from AIMS or from PARAM, depending on the set used to calibrate the relations. While the HR+AIMS relation clearly outperforms the other two, the comparison between APG17+AIMS or APG17 + PARAM suggests that using ages from individual frequencies instead of global seismic parameters have a moderate impact on calibrating chemical clocks. This is likely due to the fact that relations for chemical clocks are averaged over ages, with individual frequencies mostly improving upon precision as Fig. 4 already indicated. On the other hand, the quality of input abundances can have a considerable impact on the precision at which chemical ages can be derived.

We interpret the mean of these relative errors as a measurement of the accuracy, while the standard deviation as a measurement of the precision of chemical ages. While above we quote the relative dispersion, the absolute one, $\mathrm{Age}_{\mathrm{seismo}} - \mathrm{Age}_{\mathrm{chemical}}$, is overall independent of ages and of order of 2.95, 4.84, and 4.93 Gyr for HR+AIMS, APG17+AIMS, and APG17 + PARAM, respectively. This is highlighted by the dot-dashed line in Fig. 11 which shows the relative error in ages for an absolute uncertainty of 2.95 Gyr. Because of the inverse age trend, it is worth noticing that for ages older than about 5 Gyr relative errors are quite constant. In particular, chemical clocks calibrated onto ages from individual mode frequencies are able to deliver ages of old stars with a precision of a few tens of per cent.

4 APPLICATION TO FIELD STARS

Our final aim is to validate our relations and study their ability to provide a reliable age estimate for a larger sample of stars. We seek to verify whether the chemical ages can well reproduce key features already studied in literature, such as the age dissection of low- and high-α sequences, old metal-rich stars, and old metal-poor low-α stars and disc flaring as discussed in the following sections.

The first step is to apply our relations to the stars present in the large spectroscopic surveys APOGEE (Abdurro'uf et al. 2022) and *Gaia*-ESO (Randich et al. 2022, hereafter GES). We applied the relations at different R_g for [Ce/Mg] to APOGEE because Ce is the only *s*-process element measured in this survey, and the relations for [Zr/Ti] to the GES survey because Ce is measured in fewer stars than Zr. We also tested that the results do not qualitatively change if instead we apply the relations without binning in R_g. We would like to remind the reader that we cannot use the relations binned in R_b since we do not have information about stellar age for these stars, necessary to compute the R_b. Finally, since our sample has metallicity in the range $[-0.8, 0.2]$ dex, the chemical ages for stars out of this metallicity range are extrapolated. In the following sections, we also address the

ages extrapolated for stars beyond the range of our sample, noting that the resulting chemical ages remain within a reasonable values.

Regarding the APOGEE survey, we removed stars with the following flags: ASPCAPFLAG = STAR_WARN, STAR_BAD, STARFLAG = VERY_BRIGHT_NEIGHBOR, LOW_SNR, PERSIST_HIGH, PERSIST_JUMP_POS, PERSIST_JUMP_NEG, SUSPECT_RV_COMBINATION, and ELEMFLAG = GRIDEDGE_BAD, CALRANGE_BAD, OTHER_BAD, FERRE_FAIL for Ce. Since our observed stars are also present in the APOGEE survey, we computed the deference between our abundances and the APOGEE Stellar Parameter and Chemical Abundances Pipeline, ASPCAP, ones for Ce and Mg and [Fe/H], and we applied them to the APOGEE abundances to computed the chemical ages. Regarding the GES survey, instead, we removed stars with Zr uncertainties larger than 0.2 dex.

4.1 [α/Fe] versus [Fe/H] plane

The [α/Fe] versus [Fe/H] plane can be explained with the early, rapid contribution to the Galactic chemical enrichment by Type II supernovae, and later, long contribution by Type Ia supernovae (Tinsley 1980; Matteucci & Francois 1989; Kobayashi et al. 2006; Imig et al. 2023; Patil et al. 2023). The bimodality seen in the [α/Fe] versus [Fe/H] diagram reflects distinct formation and evolutionary histories for the two α-sequences (Chiappini, Matteucci & Gratton 1997; Chiappini 2009; Grisoni et al. 2017; Mackereth et al. 2019; Warfield et al. 2021). This can be translated into different age distributions.

Fig. 12 displays the [α/Fe] versus [Fe/H] planes for the APOGEE and GES surveys where stars in each panel are colour-coded using the chemical ages. The number of stars for which we found chemical ages is ∼ 270 000 and 1500, respectively. This is one of the largest sample with ages so far, along with the catalogues with APOGEE abundances with ages from the neural networks astroNN,[8] from the supervised machine learning technique XGBoost (Anders et al. 2023) and a catalogue with *Gaia* DR3 abundances with ages from the Bayesian isochrone-fitting code StarHorse (Nepal et al. 2024b). The panels show the separation in age for the low- and high-α sequences for both surveys: low-α stars are younger than the high-α ones and show a gradient in age increasing with α.

Furthermore, in APOGEE the separation in low- and high-α sequences is more evident than in the GES sample. However, chemical age can help us to distinguish the two sequences, even when the separation is less clear based solely on αabundances.

In the following subsections, we will just focus on the APOGEE survey since the number of stars is larger than GES. Additionally, APOGEE stars are better suited to test chrono-chemo-dynamical trends across the Galaxy, whereas GES mainly comprises stars located in the solar neighbourhood (see Queiroz et al. 2023, for a comparison of the volumes covered by different spectroscopic surveys).

4.2 [Fe/H] and [α/Fe] versus stellar age

The age–metallicity relation is a fundamental observational constraint for understanding how the Galactic disc formed and evolved chemically in time. Its existence has been a matter of debate in the past. Although a tight age–metallicity relation is known to be absent among disc stars (e.g. Edvardsson et al. 1993; Nordström et al. 2004; Haywood et al. 2013; Bergemann et al. 2014; Casagrande et al. 2016; Kruijssen et al. 2019; Mackereth et al. 2019), the increasing availability of large-scale survey data and asteroseismic ages allows us to probe its scatter and possible substructures in greater detail.

[8] https://data.sdss.org/sas/dr17/env/APOGEE_ASTRO_NN/

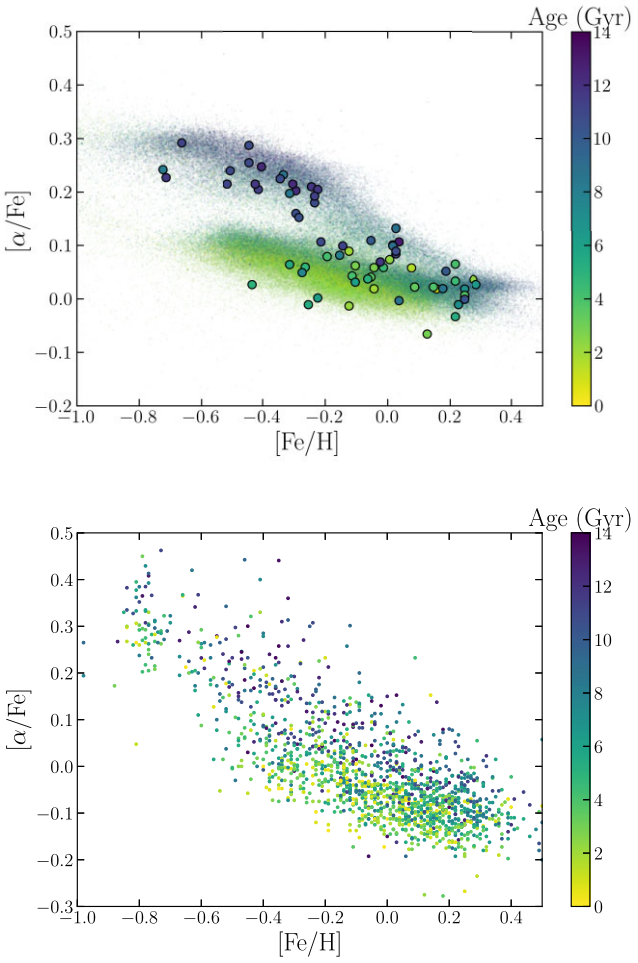

Figure 12. [α/Fe] versus [Fe/H] for field stars in the APOGEE (top) and *Gaia*-ESO (bottom panel) surveys. The stars are colour-coded by chemical ages computed using the relations for [Ce/Mg] and [Zr/Ti], respectively for the two surveys. The circles are the 68 *Kepler* stars.

In our case, we have a large number of stars with chemical age to our advantage. This is also complementary, as previous works have focused on isochrone ages of main-sequence turnoff (MSTO) and subgiant stars, while our analysis concentrated on giant stars, which are more luminous and allow the study of more distant regions. We studied, indeed, the age-metallicity relation for the APOGEE sample. The top panel of Fig. 13 shows the logarithmic chemical age versus metallicity where the stars are colour-coded with [α/Fe]. With increasingly older ages, stars show a broader range of metallicities, whereby stars with [Fe/H] < -0.6 and > 0.2 dex are consistently old. This picture is consistent with the idea that young stars form from the local ISM at roughly solar metallicity (e.g. Nieva & Przybilla 2012), whereas dynamical processes are responsible for moving more metal-poor and metal-rich stars from other locations in the Galaxy on Gyr time-scales (e.g. Schönrich & Binney 2009; Casagrande et al. 2011; Minchev, Chiappini & Martig 2013; Casagrande & VandenBerg 2014; Minchev, Chiappini & Martig 2014; Miglio et al. 2021).

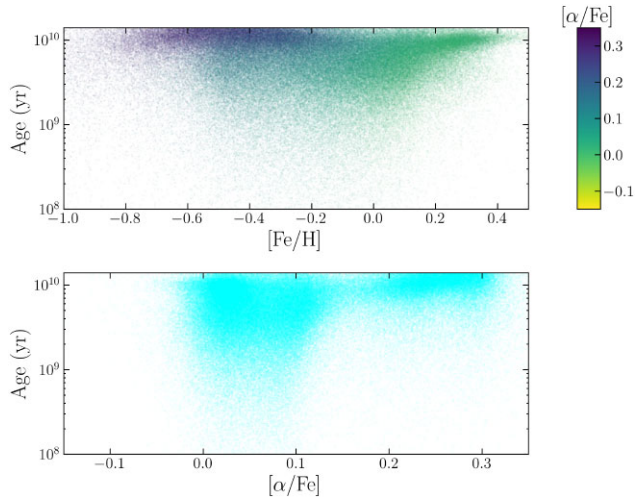

Figure 13. Top panel: logarithmic chemical age versus metallicity for the APOGEE survey where the stars are colour-coded by [α/Fe]. Bottom panel: logarithmic chemical age versus [α/Fe] for the APOGEE survey.

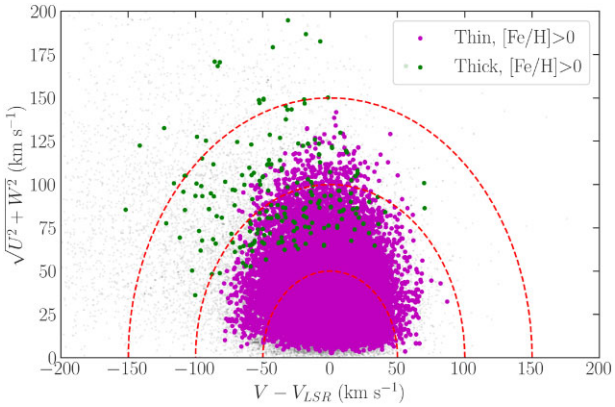

Figure 14. Toomre diagram for the APOGEE stars with [Fe/H] $>$ 0. The kinematically defined thin-disc, thick-disc stars (determined using the probability by Reddy et al. 2006) are represented as shown in the figure legend. The dashed lines indicate the total space velocity, $v_{\rm total} = \sqrt{U^2 + V^2 + W^2}$, in steps of 50 km s^{-1}. The grey dots on the background are stars with uncertainties on U, V, and W larger than 30 per cent.

The bottom panel of Fig. 13 shows the logarithmic chemical age versus [α/Fe] plane. It suggests that the chemical evolution of stars in the low-α sequence (mainly stars with [α/Fe] $<$ 0.1 dex) happened on much longer time-scales compared to the high-α sequence. In fact, the high-α stars reveal an average age of $\sim$ 11 Gyr with a narrow distribution (see also Miglio et al. 2021; Queiroz et al. 2023; Nepal et al. 2024b). The low-α stars, instead, unveil a broad age range, reaching ages as young as $\sim$ 2 Gyr and as old as the high-α sequence. This behaviour is already seen in several works, e.g. Bensby, Feltzing & Oey (2014); Hawkins et al. (2014); Miglio et al. (2021); Nepal et al. (2024b); and others.

4.3 Old metal-rich stars

In the [α/Fe] versus [Fe/H] panels, there is a bulk of old metal-rich stars (age $\gtrsim$ 8 Gyr, [Fe/H] $\gtrsim$ 0 dex), particularly evident for the APOGEE survey. The existence of old and metal-rich stars has been confirmed by several works: e.g. Trevisan et al. (2011) and Casagrande et al. (2011) using isochrone fitting; Anders et al. (2017), Miglio et al. (2021), and Alencastro Puls et al. (2023) using asteroseismic ages. These stars, often found in the thin disc, have higher metallicities despite their advanced ages, suggesting that they formed in regions of the Galaxy where star formation had already enriched the ISM with heavy elements. Their presence challenges simple models of Galactic evolution, indicating a more complex history of star formation and migration within the disc. Studies such as Chen et al. (2003); Haywood (2008); Adibekyan et al. (2011); Trevisan et al. (2011); Alencastro Puls et al. (2023); and Nepal et al. (2024a) explored the connection among age, kinematics, and metallicity, revealing that these stars could be the result of radial migration – where stars formed in the inner, metal-rich regions of the Galaxy migrate outward over time. They can be kinematically subclassified in samples of thick and thin disc stars: some of them have high eccentricity and low maximum height above the Galactic plane like thin-disc stars, while others have space velocity $V - V_{\rm LSR} < -50$ km s^{-1} (see Trevisan et al. 2011), which is more typical of a thick disc, but show solar [α/Fe] ratios that are more compatible with thin disc.

We assigned the probability of each star belonging to the kinematically defined thin and thick discs, or kinematically defined halo using the method described in Reddy, Lambert & Allende Prieto (2006). This assumes that the sample is a mixture of the three populations and their space velocities follow a Gaussian distribution. We considered that a probability larger than 70 per cent in one of the three components assigns the corresponding star to that population.

We selected stars with [Fe/H] $>$ 0 dex for the APOGEE sample and plotted them following their probabilities in the Toomre diagram as in Fig. 14. Velocities have been computed using GALPY as described in Section 2.4. In Fig. 14, we kept just stars with uncertainties on U, V, and W lower than 30 per cent. Among these metal-rich stars, most have thin-disc kinematics with a mean age of 6.8 Gyr, while only 3 per cent have thick-disc kinematics with a mean age of 7 Gyr. Moreover, they have a solar [α/Fe] ratio, belonging to the low-α sequence. This means that in a thick disc defined by kinematics, part of the stars can be low-α (see [α/Fe]–[Fe/H] planes at different positions in the Galaxy in, e.g. Anders et al. 2014; Hayden et al. 2015; Queiroz et al. 2023), underlining how the kinematically defined thick disc and chemically defined thick disc are different (see e.g. Hayden et al. 2017).

A better visualization of their distribution in age at different bins of metallicity is presented in Fig. 15. The peak of the age distribution moves from $\sim$ 5 Gyr in the most metal-poor bin to $\sim$ 10 Gyr in the most metal-rich bin. We noticed the majority of the super metal-rich stars (Miglio et al. 2021) – [Fe/H] $>$ 0.2 dex – are old. This behaviour is already seen in other works, such as Miglio et al. (2021) for giants and Nepal et al. (2024a) for MSTO and subgiants stars.

The spatial distribution of the old super metal-rich stars peaks at the solar neighbourhood in R_g, whereas their birth radii R_b (using the Lu et al.'s 2024 method and the chemical ages from [Ce/Mg]) show their origin from the inner disc (see Fig. 16). Indeed, they are too metal-rich to be a result of the star formation history of the solar vicinity, and cannot be explained by chemical evolution models which predict a maximum metallicity of [Fe/H] $\sim$ 0.2 dex in the solar neighbourhood.

4.4 Old metal-poor low-α stars

Old metal-poor low-α stars trace early accretion events in our Galaxy such as Gaia-Enceladus (Belokurov et al. 2018; Helmi et al. 2018) and Sagittarius (Ibata et al. 2001; Limberg et al. 2023) among others

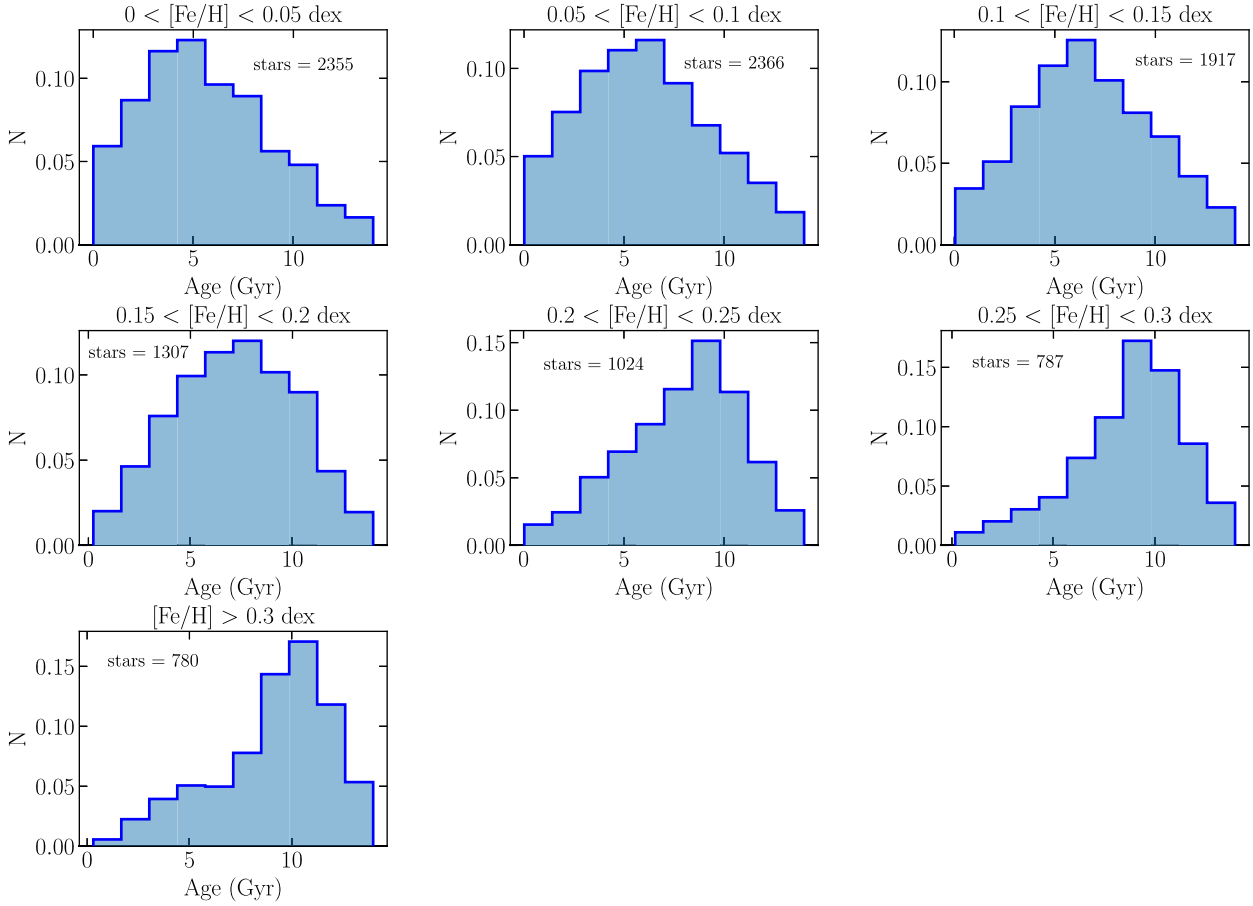

Figure 15. Chemical age distribution of APOGEE stars in different bin of metallicity ([Fe/H] > 0). *N* is a probability density as in Fig. 3. The number of stars per distribution is shown in each panel.

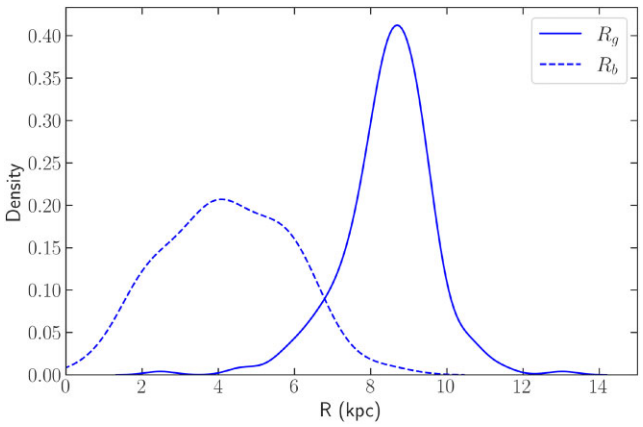

Figure 16. Spatial distribution of the APOGEE super metal-rich stars ([Fe/H] > 0.2) in R_g and R_b (computed using the chemical age from [Ce/Mg]).

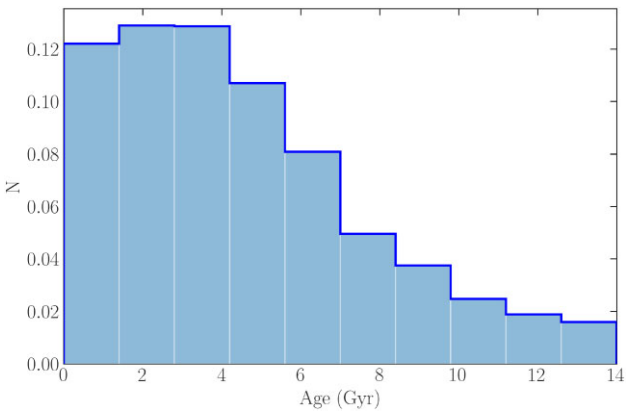

Figure 17. Chemical age distribution for the low-α [Fe/H] < −0.5 for the APOGEE stars. *N* is a probability density as in Fig. 3.

(Helmi 2020, for a review). These stars are characterized by their low metallicity and low [α/Fe] ratios, indicating that they likely formed from gas that had undergone limited enrichment from Type II supernovae, which produce α-elements, but possibly significant contributions from Type Ia supernovae, which mainly contribute to iron. Their chemical signatures suggest that they formed in environments that were chemically less enriched, potentially in smaller, accreted satellite galaxies or in isolated pockets of the early Galactic disc. Several studies have used APOGEE data to study possible accretion scenarios, such as Hasselquist et al. (2021), Horta et al. (2023), Queiroz et al. (2023), and references therein.

The age distribution of low-α [Fe/H] < −0.5 stars in Fig. 17 is composed mainly of young stars, but there is a tail towards old ages. We also identified old, low-α stars in our small sample of *Kepler* stars, with six of them exhibiting ages older than 8 Gyr at subsolar metallicity.

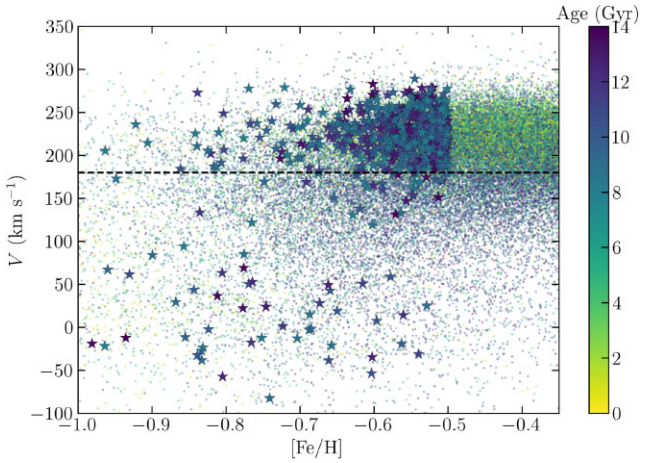

Figure 18. V versus [Fe/H] plane for the APOGEE stars colour-coded by chemical age. The star symbols are the low-α [Fe/H] < -0.5 APOGEE stars with chemical age older than 8 Gyr.

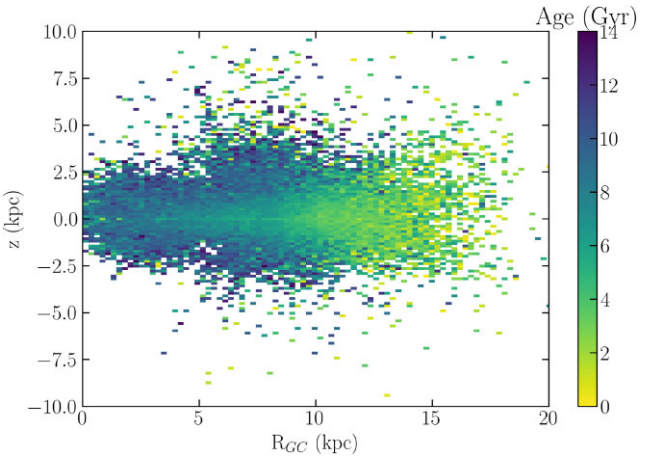

Figure 19. z versus R_{GC} plane for the APOGEE stars with [Fe/H] > -1. The distribution is colour-coded following the chemical ages computed using the [Ce/Mg]-[Fe/H]-age relations.

We selected low-α [Fe/H] < -0.5 stars from this age distribution with age older than 8 Gyr and we plotted them in the V versus [Fe/H] plane in Fig. 18 with star symbols (see discussion in Nepal et al. 2024b, and references therein). Most of them show a thin-disc kinematics ($V > 180$ km s^{-1}), while the others have a thick-disc kinematics ($V < 180$ km s^{-1}) or they are in the $V -$ [Fe/H] space designated as 'Splash' ($-0.7 <$ [Fe/H] < 0.2 dex, $V < 100$ km s^{-1}, see Belokurov et al. 2020). The presence of the old low-αmetal-poor stars suggest an early formation scenario for the Milky Way thin disc with respect to to the estimates around 8–9 Gyr, when the beginning of the formation of thin disc is dated.

4.5 Disc flaring with chemical ages

One aspect of particular interest is the phenomenon of disc flaring of our Galaxy, where young disc stars show an increasing scale height moving towards larger Galactocentric distances. This feature has been studied by several works: e.g. Miglio et al. (2013) and Stokholm et al. (2023), using seismic data; Ness et al. (2016) used [C/N] as proxy of age; works that transferred the age labels from Miglio et al. (2021), such as Leung et al. (2023), Anders et al. (2023); and finally also works as Minchev et al. (2015) and Yu et al. (2021), who have explored its implications for the structure and evolution of the Galactic disc. By applying ages from chemical clocks, we aim to contribute to this topic of interest, providing an understanding of how disc flaring relates to the age distribution of stars across different regions of the Milky Way.

Fig. 19 illustrates the R_{GC} versus z-plane (with z height on the Galactic plane), where the distribution of the stars is colour-coded with the chemical ages, as indicated by the [Ce/Mg] ratio. The values for R_{GC} and z are obtained using the GALPY package of PYTHON as in Section 2.4. The figure clearly reveals the disc flaring of the Milky Way. It shows that stars in a narrow $|z|$ range near the Galactic plane are predominantly young, with this range broadening as one moves toward the outer regions. In contrast, older stars are found at smaller R_{GC} values and are typically located farther from the plane than their younger counterparts.

The presence of the youngest stars, particularly around $z \sim 0$, suggests an ongoing star formation in the gas-enriched regions of the Galaxy. Their extension to larger radii further supports an inside–out formation scenario for the Milky Way (Matteucci & Francois 1989; Chiappini, Matteucci & Romano 2001; Grisoni, Spitoni & Matteucci 2018), where star formation initially occurred in the central regions and progressively expanded outward. This inside–out growth model is consistent with the idea that the Milky Way's disc evolved over time, with older stars remaining closer to the Galactic centre while younger stars formed in the more distant regions as the disc expanded. Through this analysis, we aim to enhance our understanding of how stellar populations and the structural evolution of the Milky Way are interconnected.

5 CONCLUSIONS

In this work, we analysed high-resolution spectra of a sample of 68 RGB *Kepler* stars, collected with HARPS-N@TNG and FIES@NOT spectrographs. We obtained precise estimates of their atmospheric parameters ($T_{\rm eff}$, $\log g$, [Fe/H], and ξ) and abundances of 25 elements. We confirmed the stellar parameters of these 68 stars found by APOGEE DR17 with optical spectra. We derived their ages through individual radial-mode frequencies, reaching an unprecedented precision (~ 8 per cent for this sample).

We used this sample of stars as calibrators for chemical clock relations. We studied mainly two chemical clocks: [Ce/Mg] and [Zr/Ti]. They show the smallest scatter related to stellar age among all abundance ratios explored in this work, maximizing the correlation with time. We investigated the relations chemical clock–[Fe/H]–age in different bins of guiding radius R_g and birth radius R_b, finding a difference less than 1σ among the parameters obtained for the inner, solar and outer regions for both radii.

The advantages of using these stars as calibrators is due to their high precision in spectroscopy and stellar age. We tested the accuracy and precision of the chemical ages derived by chemical clock–[Fe/H]–age relations, using in input both our precise abundances and the APOGEE ones. The relationships derived using the APOGEE abundances exhibit greater intrinsic scatter (~ 0.15 dex) compared to those based on the abundances measured in this work (~ 0.08 dex). As a result, these relationships yield chemical ages that differ more significantly from the asteroseismic ages, which are used as input, than when the abundances from this study are used. The result is even worst if we use in input the APOGEE abundances and less precise ages such as those derived from $\nu_{\rm max}$ and $\Delta\nu$. However, the less precise abundances affect more the relations than the less precise ages. This work demonstrates how high-precision spectroscopy and stellar age are crucial to obtain relations precise

enough to be applied to infer ages of field stars in large spectroscopic surveys. The precision present in large spectroscopy surveys such as APOGEE is not sufficient to use their abundances to obtain these empirical relations. Indeed, having chemical clock–[Fe/H]–age relations with an intrinsic scatter less than 0.1 dex and abundances with uncertainties less than 0.08 dex, as in our case, is fundamental to achieve the precision necessary to estimate chemical ages for a huge sample of stars. This level of precision is necessary if we want to have relative error in stellar ages lower than 3 Gyr across the entire Galactic chronochemical history as we showed in the Section 3.2 and Fig. 11.

Finally, we applied these relations to field stars present in the large spectroscopic surveys APOGEE and *Gaia*-ESO. Our aim was to validate this age-dating method reproducing key features of Galactic archaeology. The ages derived from chemical clocks show good agreement with results already present in the literature, such as the dichotomy in age between the high- and low-α sequences, age–metallicity relation, old metal-rich stars, old low-αstars, and disc flaring, where more precise methods have been employed. While our estimates may be less precise than, e.g. asteroseismology, they still provide a valuable contribution, particularly by increasing the statistical sample, along with other works in literature that use machine learning techniques, such as Anders et al. (2023) with XGBoost, or Leung et al. (2023) with astroNN. Moreover, these methods are especially useful when other dating techniques cannot be applied or are less effective. Therefore, the ages obtained through chemical clocks represent a valuable tool for deepening our understanding of the chemical and dynamical evolution of the Galaxy. This immediate application confirms the potential power of chemical clocks to improve our knowledge of stellar ages.

ACKNOWLEDGEMENTS

We thank Dr Alessio Mucciarelli, Dr Valentina D'Orazi, and Dr Marica Valentini for helpful discussions during the preparation of this paper. GC, AM, JS, MM, KB, VG, MT, AS, and EW acknowledge support from the European Research Council Consolidator Grant funding scheme (project ASTEROCHRONOMETRY, G.A. n. 772293, http://www.asterochronometry.eu. LM and GC acknowledge support from INAF with the Grant 'Checs, (CHEmical ClockS) Seeking a theoretical foundation for the use of chemical clocks'. LM thanks INAF for the support (Large Grant 2023 EPOCH) and the financial support under the National Recovery and Resilience Plan (NRRP), Mission 4, Component 2, Investment 1.1, Call for tender No. 104 published on 2.2.2022 by the Italian Ministry of University and Research (MUR), funded by the European Union – NextGenerationEU – Project 'Cosmic POT' grant assignment decree no. 2022X4TM3H by the Italian Ministry of Ministry of University and Research (MUR). AS acknowledges the support from the European Research Council (ERC) under the European Union's Horizon 2020 research and innovation programme (CartographY; grant agreement ID 804752). VG acknowledges financial support from INAF under the program 'Giovani Astrofisiche ed Astrofisici di Eccellenza – IAF: Astrophysics Fellowships in Italy' (Project: GalacticA, 'Galactic Archaeology: reconstructing the history of the Galaxy') and INAF Mini Grant 2023. This article is based on observations made with the Italian Telescopio Nazionale Galileo (TNG) operated on the island of La Palma by the Fundación Galileo Galilei of the INAF (Istituto Nazionale di Astrofisica) at the Spanish Observatorio del Roque de los Muchachos of the Instituto de Astrofisica de Canarias. This article is also based on observations made with the Nordic Optical Telescope, owned in collaboration by the University of Turku and Aarhus University, and operated jointly by Aarhus University, the University of Turku, and the University of Oslo, representing Denmark, Finland and Norway, the University of Iceland and Stockholm University at the Observatorio del Roque de los Muchachos, La Palma, Spain, of the Instituto de Astrofisica de Canarias. Part of the computations described in this paper were performed using the University of Birmingham's BlueBEAR HPC service, which provides a high-performance computing service to the university's research community. See http://www.birmingham.ac.uk/bear for more details.

DATA AVAILABILITY

Relevant data underlying this work are available in the article. All other data will be shared upon reasonable request to the corresponding author.

REFERENCES

Abdurro'uf et al., 2022, ApJS, 259, 35
Adibekyan V. Z., Santos N. C., Sousa S. G., Israelian G., 2011, A&A, 535, L11
Alencastro Puls A., Casagrande L., Monty S., Yong D., Liu F., Stello D., Lund M. N., 2023, MNRAS, 523, 1089
Anders F. et al., 2014, A&A, 564, A115
Anders F. et al., 2017, A&A, 600, A70
Anders F. et al., 2023, A&A, 678, A158
Asplund M., Grevesse N., Sauval A. J., Scott P., 2009, ARA&A, 47, 481
Baglin A. et al., 2006, in Fridlund M., Baglin A., Lochard J., Conroy L., eds, ESA Special Publication Vol. 1306, The CoRoT Mission Pre-Launch Status - Stellar Seismology and Planet Finding. ESA Publications, Noordwijk, p. 33
Bailer-Jones C. A. L., Rybizki J., Fouesneau M., Demleitner M., Andrae R., 2021, AJ, 161, 147
Barbuy B. et al., 2023, MNRAS, 526, 2365
Belokurov V., Erkal D., Evans N. W., Koposov S. E., Deason A. J., 2018, MNRAS, 478, 611
Belokurov V., Sanders J. L., Fattahi A., Smith M. C., Deason A. J., Evans N. W., Grand R. J. J., 2020, MNRAS, 494, 3880
Bensby T., Feltzing S., Oey M. S., 2014, A&A, 562, A71
Bergemann M. et al., 2014, A&A, 565, A89
Binney J., Tremaine S., 2008, Galactic Dynamics, Second Edition. Published by Princeton University Press, Princeton, NJ, USA
Borucki W. J. et al., 2010, Science, 327, 977
Bovy J., 2015, ApJS, 216, 29
Brogaard K. et al., 2012, A&A, 543, A106
Brogaard K. et al., 2018, MNRAS, 476, 3729
Brogaard K. et al., 2022, A&A, 668, A82
Busso M., Gallino R., Lambert D. L., Travaglio C., Smith V. V., 2001, ApJ, 557, 802
Cantat-Gaudin T. et al., 2014, A&A, 562, A10
Casagrande L. et al., 2016, MNRAS, 455, 987
Casagrande L., Flynn C., Portinari L., Girardi L., Jimenez R., 2007, MNRAS, 382, 1516
Casagrande L., Schönrich R., Asplund M., Cassisi S., Ramírez I., Meléndez J., Bensby T., Feltzing S., 2011, A&A, 530, A138
Casagrande L., VandenBerg D. A., 2014, MNRAS, 444, 392
Casali G. et al., 2020, A&A, 639, A127
Casali G. et al., 2023, A&A, 677, A60
Casamiquela L. et al., 2021, A&A, 652, A25
Chaplin W. J., Miglio A., 2013, ARA&A, 51, 353
Chen Y. Q., Zhao G., Nissen P. E., Bai G. S., Qiu H. M., 2003, ApJ, 591, 925
Chiappini C., 2009, in Andersen J., Bland-Hawthorn J., Nordström B., eds, IAU Symp. Vol. 254, The Galaxy Disk in Cosmological Context, p. 191
Chiappini C., Matteucci F., Gratton R., 1997, ApJ, 477, 765
Chiappini C., Matteucci F., Romano D., 2001, ApJ, 554, 1044
Cosentino R. et al., 2012, in McLean I. S., Ramsay S. K., Takami H.eds, Proc. SPIE Conf. Ser.Vol. 8446, Ground-based and Airborne Instrumentation for Astronomy IV, p. 84461V

Cristallo S., Straniero O., Piersanti L., Gobrecht D., 2015, ApJS, 219, 40
Cunha K. et al., 2017, ApJ, 844, 145
da Silva L. et al., 2006, A&A, 458, 609
da Silva R., Porto de Mello G. F., Milone A. C., da Silva L., Ribeiro L. S., Rocha-Pinto H. J., 2012, A&A, 542, A84
Davies G. R., Miglio A., 2016, Astron. Nachr., 337, 774
De Silva G. M. et al., 2015, MNRAS, 449, 2604
Delgado Mena E. et al., 2019, A&A, 624, A78
Edvardsson B., Andersen J., Gustafsson B., Lambert D. L., Nissen P. E., Tomkin J., 1993, A&A, 275, 101
Feltzing S., Howes L. M., McMillan P. J., Stonkutė E., 2017, MNRAS, 465, L109
Gaia Collaboration, 2021, A&A, 649, A1
Gallart C. et al., 2024, A&A, 687, A168
Gilliland R. L. et al., 2010, PASP, 122, 131
Grisoni V., Spitoni E., Matteucci F., 2018, MNRAS, 481, 2570
Grisoni V., Spitoni E., Matteucci F., Recio-Blanco A., de Laverny P., Hayden M., Mikolaitis Ŝ., Worley C. C., 2017, MNRAS, 472, 3637
Gustafsson B., Edvardsson B., Eriksson K., Jørgensen U. G., Nordlund Å., Plez B., 2008, A&A, 486, 951
Handberg R., Brogaard K., Miglio A., Bossini D., Elsworth Y., Slumstrup D., Davies G. R., Chaplin W. J., 2017, MNRAS, 472, 979
Hasselquist S. et al., 2021, ApJ, 923, 172
Hawkins K., Jofré P., Gilmore G., Masseron T., 2014, MNRAS, 445, 2575
Hayden M. R. et al., 2015, ApJ, 808, 132
Hayden M. R., Recio-Blanco A., de Laverny P., Mikolaitis S., Worley C. C., 2017, A&A, 608, L1
Hayes C. R. et al., 2022, ApJS, 262, 34
Haywood M., 2008, MNRAS, 388, 1175
Haywood M., Di Matteo P., Lehnert M. D., Katz D., Gómez A., 2013, A&A, 560, A109
Hegedűs V., Mészáros S., Jofré P., Stringfellow G. S., Feuillet D., García-Hernández D. A., Nitschelm C., Zamora O., 2023, A&A, 670, A107
Heiter U. et al., 2015, Phys. Scr., 90, 054010
Heiter U. et al., 2021, A&A, 645, A106
Helmi A., 2020, ARA&A, 58, 205
Helmi A., Babusiaux C., Koppelman H. H., Massari D., Veljanoski J., Brown A. G. A., 2018, Nature, 563, 85
Horta D. et al., 2023, MNRAS, 520, 5671
Howell S. B. et al., 2014, PASP, 126, 398
Huber D. et al., 2011, ApJ, 743, 143
Huber D. et al., 2013, ApJ, 767, 127
Ibata R., Irwin M., Lewis G. F., Stolte A., 2001, ApJ, 547, L133
Imig J. et al., 2023, ApJ, 954, 124
Jofré P., Jackson H., Tucci Maia M., 2020, A&A, 633, L9
Jönsson H. et al., 2020, AJ, 160, 120
Jørgensen A. C. S. et al., 2021, MNRAS, 500, 4277
Jurić M. et al., 2008, ApJ, 673, 864
Kobayashi C., Umeda H., Nomoto K., Tominaga N., Ohkubo T., 2006, ApJ, 653, 1145
Kruijssen J. M. D., Pfeffer J. L., Reina-Campos M., Crain R. A., Bastian N., 2019, MNRAS, 486, 3180
Lebreton Y., Goupil M. J., 2014, A&A, 569, A21
Leung H. W., Bovy J., Mackereth J. T., Miglio A., 2023, MNRAS, 522, 4577
Lillo-Box J. et al., 2014, A&A, 562, A109
Limberg G. et al., 2023, ApJ, 946, 66
Lu Y. L. et al., 2024, MNRAS, 535, 392
Lynden-Bell D., Kalnajs A. J., 1972, MNRAS, 157, 1
Mackereth J. T. et al., 2019, MNRAS, 489, 176
Mackereth J. T. et al., 2021, MNRAS, 502, 1947
Magrini L. et al., 2013, A&A, 558, A38
Magrini L. et al., 2021, A&A, 646, L2
Majewski S. R. et al., 2017, AJ, 154, 94
Matteucci F., Francois P., 1989, MNRAS, 239, 885
Miglio A. et al., 2013, MNRAS, 429, 423
Miglio A. et al., 2021, A&A, 645, A85
Minchev I., Chiappini C., Martig M., 2013, A&A, 558, A9
Minchev I., Chiappini C., Martig M., 2014, A&A, 572, A92
Minchev I., Martig M., Streich D., Scannapieco C., de Jong R. S., Steinmetz M., 2015, ApJ, 804, L9
Montalbán J. et al., 2021, Nat. Astron., 5, 640
Nepal S. et al., 2024a, A&A, 681, L8
Nepal S., Chiappini C., Queiroz A. B., Guiglion G., Montalbán J., Steinmetz M., Miglio A., Khalatyan A., 2024b, A&A, 688, A167
Ness M., Hogg D. W., Rix H. W., Martig M., Pinsonneault M. H., Ho A. Y. Q., 2016, ApJ, 823, 114
Nieva M. F., Przybilla N., 2012, A&A, 539, A143
Nissen P. E., 2015, A&A, 579, A52
Nissen P. E., Christensen-Dalsgaard J., Mosumgaard J. R., Silva Aguirre V., Spitoni E., Verma K., 2020, A&A, 640, A81
Nordström B. et al., 2004, A&A, 418, 989
Patil A. A., Bovy J., Jaimungal S., Frankel N., Leung H. W., 2023, MNRAS, 526, 1997
Pinsonneault M. H. et al., 2025, ApJS, 276, 69
Queiroz A. B. A. et al., 2023, A&A, 676, C6
Randich S. et al., 2022, A&A, 666, A121
Ratcliffe B. et al., 2023, MNRAS, 525, 2208
Reddy B. E., Lambert D. L., Allende Prieto C., 2006, MNRAS, 367, 1329
Reese D. R., 2016, Astrophysics Source Code Library, recordascl:1611.014
Rendle B. M. et al., 2019, MNRAS, 484, 771
Ricker G. R. et al., 2014, in Oschmann Jacobus M. J., Clampin M., Fazio G. G., MacEwen H. A., eds, Proc. SPIE Conf. Ser., Vol. 9143, Space Telescopes and Instrumentation 2014: Optical, Infrared, and Millimeter Wave, p. 914320, preprint (arXiv:1406.0151)
Rodrigues T. S. et al., 2017, MNRAS, 467, 1433
Sales-Silva J. V. et al., 2022, ApJ, 926, 154
Sales-Silva J. V. et al., 2024, ApJ, 965, 119
Schonhut-Stasik J. et al., 2024, AJ, 167, 50
Schönrich R., Binney J., 2009, MNRAS, 399, 1145
Schönrich R., Binney J., Dehnen W., 2010, MNRAS, 403, 1829
Sellwood J. A., Binney J. J., 2002, MNRAS, 336, 785
Shejeelammal J., Meléndez J., Rathsam A., Martos G., 2024, A&A, 690, A107
Silva Aguirre V. et al., 2017, ApJ, 835, 173
Slumstrup D., Grundahl F., Brogaard K., Thygesen A. O., Nissen P. E., Jessen-Hansen J., Van Eylen V., Pedersen M. G., 2017, A&A, 604, L8
Sneden C., Bean J., Ivans I., Lucatello S., Sobeck J., 2012, Astrophysics Source Code Library, recordascl:1202.009
Soderblom D. R., 2010, ARA&A, 48, 581
Spina L. et al., 2018, MNRAS, 474, 2580
Spina L., Meléndez J., Karakas A. I., Ramírez I., Monroe T. R., Asplund M., Yong D., 2016, A&A, 593, A125
Stetson P. B., Pancino E., 2008, PASP, 120, 1332
Stokholm A., Aguirre Børsen-Koch V., Stello D., Hon M., Reyes C., 2023, MNRAS, 524, 1634
Telting J. H. et al., 2014, Astron. Nachr., 335, 41
Thomsen J. S. et al., 2025, preprint (arXiv:2504.17853)
Tinsley B. M., 1980, Fund. Cosmic Phys., 5, 287
Trevisan M., Barbuy B., Eriksson K., Gustafsson B., Grenon M., Pompéia L., 2011, A&A, 535, A42
Verma K., Raodeo K., Basu S., Silva Aguirre V., Mazumdar A., Mosumgaard J. R., Lund M. N., Ranadive P., 2019, MNRAS, 483, 4678
Vescovi D., Cristallo S., Busso M., Liu N., 2020, ApJ, 897, L25
Viscasillas Vázquez C. et al., 2022, A&A, 660, A135
Vrard M., Mosser B., Samadi R., 2016, A&A, 588, A87
Warfield J. T. et al., 2021, AJ, 161, 100
Warfield J. T. et al., 2024, AJ, 167, 208
Yu Y. et al., 2021, ApJ, 922, 80

This paper has been typeset from a TEX/LATEX file prepared by the author.